Computers and Structures 322 (2026) 108116

Contents lists available at ScienceDirect

Computers and Structures

journal homepage: www.elsevier.com/locate/cas

# Modelling interface damage in masonry structures under cyclic loading conditions with cohesive fracture and regularized friction

G. Cera [a, b, *], J.G. Rots [a], A.T. Slobbe [b], F. Messali [a]

[a] Delft University of Technology, Faculty of Civil Engineering and Geosciences, Delft, Netherlands
[b] Netherlands Organization for Applied Scientific Research (TNO), Delft, Netherlands

ARTICLE INFO

*Keywords:*
Unreinforced masonry
Simplified micromodelling
Cohesive zone model
Mixed-mode fracture
Friction
Cyclic loading

ABSTRACT

An existing interface material model for quasi-brittle fracture, originally developed within the Discrete Element Method framework, is implemented and enhanced for use in implicit Finite Element analyses of unreinforced masonry structures. The model captures mixed-mode fracture in tension-shear and combines cohesion with Coulomb friction in compression-shear. To address convergence issues arising when loading–unloading takes place, due to a discontinuity in the traction–separation relation, a regularization of the frictional contribution is proposed. A new model parameter is introduced and a calibration procedure to ensure numerical robustness and objectivity is presented. Furthermore, the consistent tangent stiffness matrix is derived to improve convergence in full-scale simulations. The improved model is applied within a simplified micromodelling approach to simulate the in-plane cyclic response of 2D masonry structures, including a shear wall and a spandrel subjected to a combination of horizontal and vertical actions. The results demonstrate that the model accurately reproduces key aspects of masonry behaviour, including stiffness degradation, energy dissipation, and crack patterns, while maintaining robustness and efficiency in complex cyclic loading scenarios.

## 1. Introduction

The vast majority of historical structures and a large portion of old dwellings in Europe are composed of unreinforced masonry (URM), a construction technique that, while historically significant, is particularly vulnerable to damage. Mechanical stresses, environmental degradation and natural hazards, such as earthquakes, pose serious threats to the integrity of these buildings. Therefore, there is need for advanced numerical methods to accurately and efficiently assess their structural condition and ensure their preservation for future generations.

Masonry is a composite material consisting of units and dry or mortar joints. Its response is strongly nonlinear and depends on the response of each constituent, their arrangement within the structure and the quality of their bond. Due to the highly asymmetric behaviour in tension and compression of this material, URM buildings are designed to work in compression [1], resulting in vulnerability to both horizontal loads (earthquakes [2,3]) and differential settlements (tunnelling, excavations, mining, cyclic seasonal effects [3–7]). Depending on the origin of the loads, structures can be subjected to monotonic or cyclic actions. The simulation of the latter is particularly challenging since, under cyclic loading, masonry exhibits both damage accumulation and permanent deformations, leading to a complex unloading-reloading response.

Various modelling approaches have been applied to simulate masonry behaviour. Among these, brick-to-brick micromodels represent masonry on the scale of its main heterogeneity. These models, despite their high computational cost, are frequently used when an accurate description of the response of masonry is required. A distinction can be made between detailed and simplified micromodels [8], see Fig. 1. The former explicitly describe bricks and mortar joints as (linear or nonlinear) continuum elements and allow discontinuities in the displacement field by placing zero-thickness interfaces between the bricks and the mortar. In contrast, simplified micromodels describe masonry as being made of elastic or inelastic bricks with expanded geometry and allow the formation of potential cracks by placing zero-thickness interfaces that account for the behaviour of both the mortar and the brick-mortar interaction. By not explicitly modelling the mortar joints, this approach enables the use of a coarser mesh and generally provides a better balance between accuracy and analysis time.

Interface elements provide a realistic description of cracks modelled as geometric discontinuities. Their constitutive relation describes the

* Corresponding author at: Delft University of Technology, Faculty of Civil Engineering and Geosciences, Delft, Netherlands.
*Email address:* g.cera@tudelft.nl (G. Cera).

https://doi.org/10.1016/j.compstruc.2026.108116
Received 29 September 2025; Accepted 11 January 2026
Available online 29 January 2026

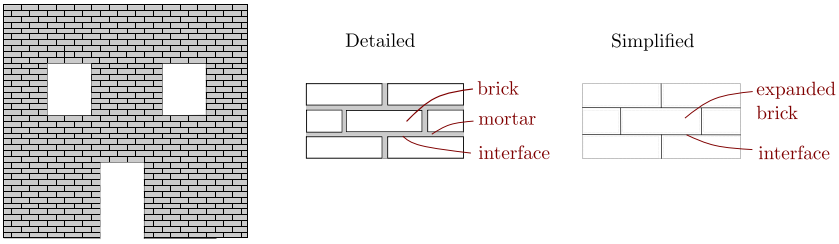


**Fig. 1.** Masonry micromodelling (adapted from [9]).

progressive separation of the two crack faces that occurs in the *fracture process zone* through a cohesive relation formulated within the framework of damage or plasticity [10,11]. This representation is widely used for studying the initiation and propagation of cracks in various composite materials and is particularly appealing for modelling brickwork masonry, since the regularity of its texture generates preferred fracture planes. These weak paths are frequently determined by the joint layers [12].

A significant number of interface constitutive models have been developed to investigate the response of different materials, such as rocks, concrete and fibre reinforced composites [13–17]. Starting from the work of Page [18], interface material models have been proposed for the micromodelling of masonry structures. In this context, several contributions have been formulated in a plasticity framework [19–27]. Lotfi and Shing [19] presented a non-associative plasticity-based interface material model for the analysis of masonry panels. Lourenço and Rots [21] proposed a multi-surface plasticity model, which simulates cracking, joint slip and crushing. To capture the local failure mechanisms of masonry within the interfaces, this model was used in combination with quasi-brittle interfaces, located inside elastic units, to describe the potential splitting of the bricks [20]. Plasticity-based formulations offer the advantage of readily accounting for masonry dilatancy [19,21,23,24,27]. However, by displaying an elastic unloading, they are not directly suitable for describing the complex behaviour of masonry under cyclic actions.

To describe the cyclic response of materials that exhibit both stiffness degradation and permanent displacements, formulations combining damage and friction have been developed [28–33]. Interesting contributions have proposed smooth transitions from a cohesive to a frictional response [29–33]. In particular, a physically-based approach to combine cohesion and friction was proposed by Raous and Monerie [30] and Alfano and Sacco [31]. These authors distinguished between an undamaged and damaged area. By allowing the friction to act only on the latter, cohesive and frictional behaviours were combined through a measure of the interface damage. This idea has been applied to studying the cohesive-frictional interaction of masonry material at different scales, ranging from small samples to walls and arches [34–36].

More recently, Venzal et al. [35] presented an interface material model for quasi-brittle fracture in the context of the Discrete Element Method (DEM), which combines cohesion and Coulomb friction in compression-shear [31] and accounts for mixed-mode fracture in tension-shear [37]. This interface material model, which requires only a few model parameters for its characterization, was used in a detailed micromodelling description to simulate a small masonry assemblage (triplet test). Boukham et al. [38] extended the model in [35] and presented a hybrid approach, combining the Discrete and Finite Element Methods (DEM-FEM). The model consists of non-expanded bricks described by plastic-damage finite elements, while an extension of Venzal's interface model is used to simulate the behaviour of the elastic mortars and the brick-mortar interaction. This DEM-FEM approach was applied to study a masonry shear-wall subjected to monotonic loading. So far, the performance of Venzal's interface model has not been tested on a full-scale wall subjected to cyclic loads.

In this work, the interface material model proposed by Venzal et al. [35] is extended for use in an implicit scheme and applied for the first time to analyses of full-scale masonry structures subjected to cyclic loadings. To this end, the formulation in [35] is implemented in an implicit finite element framework and improved to increase the robustness and the efficiency of the analyses. Specifically, a regularization of the frictional term [39] is proposed to enhance the convergence behaviour of Venzal's model, thereby enabling the simulation of full-scale structures. Furthermore, the traction update algorithm is consistently linearized for efficient analyses. These enhancements enable to simulate the post-peak response of full-scale masonry structures with the micromodelling approach, while retaining computational efficiency.

The paper is organized as follows. Venzal's interface constitutive model is described in Section 2.1. Details about the regularization of the frictional term are presented in Section 2.2, and the consistent tangent stiffness matrix is derived in Section 2.3. In Section 3, the model is validated against a cyclic shear wall experiment, and the robustness and efficiency of the model are demonstrated in Section 4 through the simulation of a complex spandrel laboratory test subjected to differential settlements. Finally, the conclusions are discussed in Section 5.

## 2. Frictional cohesive zone model

### 2.1. Venzal's interface material model

Venzal's interface material model [35] accounts for mixed-mode cohesive fracture in tension-shear, and combines cohesive fracture and friction in compression-shear. A schematic representation of the model is provided in Fig. 2. In tension, both mode I and mode II components of the response are cohesive and characterized by exponential softening. In compression, the response in mode I is elastic, while in mode II the response is frictional-cohesive, see Fig. 3. This combination is based on the physical idea that, in the interface, it is possible to discern between an undamaged and a damaged area ($A_{\mathrm{u}}$ and $A_{\mathrm{d}}$ respectively), with the cohesion acting on $A_{\mathrm{u}}$ and the friction on $A_{\mathrm{d}}$ [30,31].

An interface damage variable is introduced as a measure of the damaged area with respect to the total area:

$$d = \frac{A_{\mathrm{d}}}{A_{\mathrm{u}} + A_{\mathrm{d}}}, \quad d \in [0, 1] \tag{1}$$

The total traction $\mathbf{t}$ consists of two contributions, $\mathbf{t}_{\mathrm{coh}}$ and $\mathbf{t}_{\mathrm{fric}}$, which represent the cohesive and frictional parts, respectively:

$$\mathbf{t} = \mathbf{t}_{\mathrm{coh}} + f_{\mathrm{d}}(d)\,\mathbf{t}_{\mathrm{fric}} \tag{2}$$

In this equation, the function $f_{\mathrm{d}}(d)$ regulates the interaction between the two contributions.

The interface material model is formulated in a local reference system, with normal and shear components (denoted by the subscripts n and s) oriented in the normal and tangential directions with respect to the interface geometry, respectively (Fig. 2, *right*). In this local frame, the traction and displacement jump vectors, $\mathbf{t}$ and $[\![\mathbf{u}]\!]$, are expressed as:

$$\mathbf{t} = \left[t_{\mathrm{n}},\, t_{\mathrm{s}}\right]^{\mathrm{T}} \qquad [\![\mathbf{u}]\!] = \left[[\![u]\!]_{\mathrm{n}},\, [\![u]\!]_{\mathrm{s}}\right]^{\mathrm{T}} \tag{3}$$

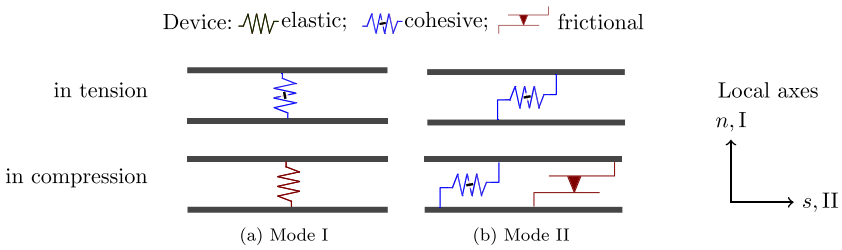


**Fig. 2.** Schematic representation of Venzal's model for mode I and mode II components of the response: in tension (*top*) and compression (*bottom*).

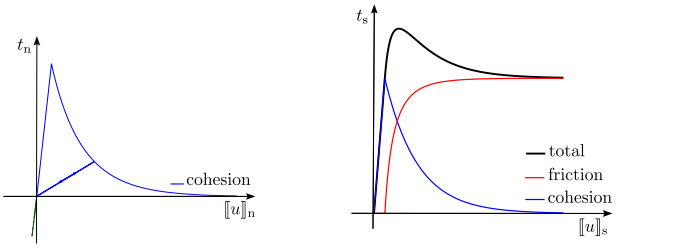


(a) Traction opening - crack opening

(b) Traction shearing - shear sliding (friction is enabled for $t_n \leq 0$ and is depicted for $t_n = \text{const}$)

**Fig. 3.** Traction-separation curves in mode I (a) and mode II (b).

The constitutive equation that relates the total traction, Eq. (2), to the displacement jump is

$$\mathbf{t} = \underbrace{(\mathbf{I} - d\,\mathbf{P})\,\mathbf{K}[\![\mathbf{u}]\!]}_{\mathbf{t}_{\text{coh}}} + f_{\text{d}}(d)\,\underbrace{\operatorname{sgn}\left(\Delta[\![u]\!]_{\text{s}}\right)\mu\, k_{\text{n}}\langle -[\![u]\!]_{\text{n}}\rangle\,[0,1]^{\text{T}}}_{\mathbf{t}_{\text{fric}}}, \quad d \in [0,1] \tag{4}$$

where $\mathbf{I}$ is the identity matrix. The matrices $\mathbf{K}$ and $\mathbf{P}$ are specified as:

$$\mathbf{K} = \begin{bmatrix} k_{\text{n}} & 0 \\ 0 & k_{\text{s}} \end{bmatrix}; \qquad \mathbf{P} = \begin{bmatrix} \frac{\langle [\![u]\!]_{\text{n}} \rangle}{[\![u]\!]_{\text{n}}} & 0 \\ 0 & 1 \end{bmatrix} \tag{5}$$

with $k_{\text{n}}$ and $k_{\text{s}}$ denoting the initial values of the elastic stiffness in pure modes and $\langle x \rangle = \max(0, x)$. The function $\operatorname{sgn}\left(\Delta[\![u]\!]_{\text{s}}\right)$ determines the direction of the frictional term while the symbol $\mu$ indicates the friction coefficient that accounts in a simplified way for the roughness of the damaged area $A_{\text{d}}$. Each contribution in Eq. (4), cohesive and frictional, is individually explained in the following.

### 2.1.1. Cohesive contribution to traction

Under tension-shear, the response is purely cohesive as illustrated in Fig. 2. In mode I, the matrix $\mathbf{P}$ accounts for the unilateral response of masonry: the model shows a reduction in the stiffness in tension during damage growth, while it recovers the initial elastic stiffness in compression upon crack re-closure.

The model accounts for mixed-mode cohesive fracture through a mixed-mode ratio $\beta$ [37]. The definition of $\beta$ has been modified with respect to [35] where it was defined as $\beta = [\![u]\!]_{\text{s}} / [\![u]\!]_{\text{n}}$ and ranged from 0 (pure-mode I) to $\pm\infty$ (pure-mode II). In this work, to avoid numerical instability, the mixed-mode ratio is expressed as [40]:

$$\beta = \frac{[\![u]\!]_{\text{s}}^2}{\langle [\![u]\!]_{\text{n}} \rangle^2 + [\![u]\!]_{\text{s}}^2} \tag{6}$$

and ranges from 0 (pure-mode I) to 1 (pure-mode II).[1] The equivalent displacement jump in mixed-mode is defined as:

$$[\![u]\!]_{\text{eq}} = \sqrt{\langle [\![u]\!]_{\text{n}} \rangle^2 + [\![u]\!]_{\text{s}}^2} \tag{7}$$

[1] The re-definition of the mixed-mode ratio $\beta$ leads to changes in the mixed-mode equations with respect to [35]. A more extensive explanation of the cohesive equations is presented in Appendix A.

In the case of mode-mixity, the onset of a developing cohesive crack is established through a damage initiation criterion. In particular, a quadratic relation is used [41]:

$$\left(\frac{\langle t_{\text{n}} \rangle}{f_{\text{n}}}\right)^2 + \left(\frac{t_{\text{s}}}{f_{\text{s}}}\right)^2 = 1 \tag{8}$$

with $f_{\text{n}}$ and $f_{\text{s}}$ denoting the strengths in pure-mode I and II, respectively (Fig. 4a). Furthermore, the mixed-mode cohesive fracture energy $G_{\text{f,mix}}$ is given as:

$$\left(\frac{G_{\text{f,mix,I}}}{G_{\text{f,I}}}\right)^{\alpha} + \left(\frac{G_{\text{f,mix,II}}}{G_{\text{f,II}}}\right)^{\alpha} = 1 \tag{9}$$

where $G_{\text{f},i}$, $i = \text{I, II}$ indicate the pure-mode fracture energies and $G_{\text{f,mix},i}$, $i = \text{I, II}$ denote the pure-mode components of the mixed-mode fracture energy $G_{\text{f,mix}}$ (Fig. 4b). The interaction between mode I and II components is regulated by the parameter $\alpha$. The damage initiation criterion, Eq. (8), leads to the expressions for the mixed-mode strength $f_{\text{m}}$ and the corresponding mixed-mode displacement jump $[\![u]\!]_{\text{m}}$:

$$f_{\text{m}} = [\![u]\!]_{\text{n}}^{\text{e}} [\![u]\!]_{\text{s}}^{\text{e}} \sqrt{\frac{(1-\beta)\,k_{\text{n}}^2 + \beta\, k_{\text{s}}^2}{\beta\left([\![u]\!]_{\text{n}}^{\text{e}}\right)^2 + (1-\beta)\left([\![u]\!]_{\text{s}}^{\text{e}}\right)^2}} \tag{10}$$

$$[\![u]\!]_{\text{m}} = [\![u]\!]_{\text{n}}^{\text{e}} [\![u]\!]_{\text{s}}^{\text{e}} \sqrt{\frac{1}{\beta\left([\![u]\!]_{\text{n}}^{\text{e}}\right)^2 + (1-\beta)\left([\![u]\!]_{\text{s}}^{\text{e}}\right)^2}} \tag{11}$$

where $[\![u]\!]_{\text{n}}^{\text{e}}$ and $[\![u]\!]_{\text{s}}^{\text{e}}$ are the limit elastic values of the displacement jump for each mode. From Eqs. (10) and (11) the initial stiffness in mixed-mode can be computed:

$$k = \frac{f_{\text{m}}}{[\![u]\!]_{\text{m}}} \tag{12}$$

The mixed-mode fracture energy $G_{\text{f,mix}}$ is evaluated from its pure-mode components $G_{\text{f,mix},i}$, $i = \text{I,II}$:

$$G_{\text{f,mix}} = G_{\text{f,mix,I}} + G_{\text{f,mix,II}} \tag{13}$$

where

$$G_{\text{f,mix},i} = \psi_i\, G_{\text{f},i} \qquad i = \text{I, II} \tag{14}$$

with $\psi_i$, $i = \text{I, II}$ denoting the ratio of the mixed-mode components of the fracture energy with respect to the pure-mode fracture energies, which are expressed as:

$$\psi_{\text{I}} = \frac{(1-\beta)\left([\![u]\!]_{\text{s}}^{\text{e}}\right)^2}{(1-\beta)\left([\![u]\!]_{\text{s}}^{\text{e}}\right)^2 + \beta\left([\![u]\!]_{\text{n}}^{\text{e}}\right)^2}; \qquad \psi_{\text{II}} = \frac{\beta\left([\![u]\!]_{\text{n}}^{\text{e}}\right)^2}{(1-\beta)\left([\![u]\!]_{\text{s}}^{\text{e}}\right)^2 + \beta\left([\![u]\!]_{\text{n}}^{\text{e}}\right)^2} \tag{15}$$

Consequently, the failure criterion, Eq. (9), can be rewritten as:

$$\psi_{\text{I}} + \psi_{\text{II}} = 1 \tag{16}$$

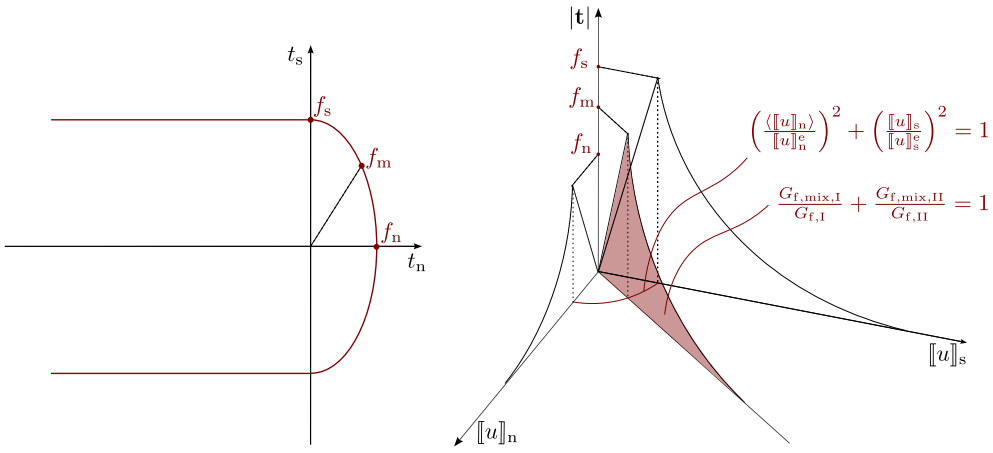


(a) Damage initiation criterion (in terms of traction components)

(b) Damage initiation (in terms of displacement jump components) and failure criteria

**Fig. 4.** Cohesive mixed-mode formulation (the mixed-mode response is depicted for $\beta = \text{const}$).

Finally, the scalar damage parameter $d$ in Eq. (4) at the current load-step, is given as [35]:

$$d = \max\left\{ d_0,\ 1 - \left(\frac{f_m}{k\,[\![u]\!]_{eq}}\right) \exp\left(\phi\left(\frac{f_m}{k} - [\![u]\!]_{eq}\right)\right)\right\}, \quad d \in [0,1] \tag{17}$$

where $d_0$ is the damage at the last converged load-step. The parameter $d$ monotonically increases and depends on the mixed-mode quantities $[\![u]\!]_{eq}$, $f_m$, $[\![u]\!]_m$, $k$ and $\phi$. The function $\phi$ ensures that the fracture energy, dissipated upon complete decohesion of the interface unit area, corresponds to $G_{f,mix}$ [35]:

$$\phi = \frac{2\,k\,f_m}{2\,k\,G_{f,mix} - f_m^2} \tag{18}$$

The expression for the damage variable, Eq. (17), corresponds to an exponential softening response [35].

#### 2.1.2. Frictional contribution to traction

Under compression-shear, the mode II component is frictional-cohesive (Fig. 2). The function $f_d(d)$ that governs this interaction, Eq. (4), is defined as [35]:

$$f_d(d) = d^p, \qquad p \geq 1 \tag{19}$$

where $p$ is a coupling parameter, which controls the interaction between cohesion and friction. Its effect on the response is studied in Section 3. If the material is pristine ($d = 0$), the response is elastic (Fig. 5a), whereas after the strength of the material is reached and the damage occurs ($0 < d < 1$), the cohesive response goes into softening and a frictional response arises on the damaged part of the interface (Fig. 5b). When the interface reaches complete decohesion, its response is fully frictional (Fig. 5c). Note that coupling cohesion and friction through a function that depends on the damage $d$ allows for a smooth transition from a purely cohesive behaviour to a purely frictional one, as illustrated in Fig. 6.

Finally, in Eq. (4), the expression $\mu\,k_n\langle -[\![u]\!]_n\rangle$ defines the magnitude of the Coulomb friction, while the function $\text{sgn}\left(\Delta[\![u]\!]_s\right)$ determines its direction. In general, friction acts in the opposite direction to the relative sliding motion between two bodies or, specifically for the case at hand, between the faces of a crack. In the interface material model, the sign of the frictional term is determined by the local sign of the sliding displacement jump increment, $\Delta[\![u]\!]_s$. Therefore, a change in the direction of the relative motion, which, at the integration point level, can be due to stress redistribution in the structure (*e.g.,* when damage occurs), can lead to a switch in the local sign of the frictional contribution. When this occurs, the total traction experiences an abrupt change in its value, with magnitude $2\mu|t_n|$, as illustrated in Fig. 7.

The function $\text{sgn}\left(\Delta[\![u]\!]_s\right)$, in Eq. (4), introduces a strong discontinuity (jump) in the constitutive relation. For $\Delta[\![u]\!]_s = 0$ (singularity point) the tangent stiffness matrix is undefined. Consequently, during global iterations, the absence of a proper definition of the tangent modulus can lead to oscillations at the sign of the frictional term, in the integration points where $|\Delta[\![u]\!]_s| \ll 1$. This can ultimately cause a loss of convergence in the analysis, as will be demonstrated with a numerical example in Section 3.2. To increase the robustness of the model, a regularization of the frictional term is proposed in the next section.

### 2.2. Proposed regularization of the frictional contribution

To improve the convergence behaviour of Venzal's model, a modification to the definition of the frictional term is proposed. Specifically, the discontinuous function $\text{sgn}\left(\Delta[\![u]\!]_s\right)$, Eq. (4), is replaced by one of its smooth approximations $h_s$ [39]:

$$\text{sgn}\left(\Delta[\![u]\!]_s\right) \approx \underbrace{\tanh\left(\vartheta\,\Delta[\![u]\!]_s\right)}_{h_s}, \qquad h_s \in C^\infty \tag{20}$$

The use of the differentiable function $h_s$ allows a proper definition of the tangent modulus. However, it introduces a new model parameter $\vartheta$, which regulates the steepness of $h_s$ and requires calibration, see Fig. 8. In particular, a larger value of the regularization parameter $\vartheta$ provides a better approximation of the sign function. In the limit, the smooth function $h_s$ converges to the discontinuous function sign:

$$\lim_{\vartheta\to\infty} \tanh(\vartheta\Delta[\![u]\!]_s) = \text{sgn}(\Delta[\![u]\!]_s) \tag{21}$$

The performance of the proposed formulation and the effect on the response of varying the regularization parameter, $\vartheta$, are investigated in Section 3.2.

### 2.3. Derivation of the algorithmic tangent stiffness matrix

For implicit finite element analyses, the definition of the algorithmic tangent stiffness matrix is crucial to efficiently achieve convergence in full-scale analyses. In this section, the traction update is consistently linearized. The traction-separation relation, Eq. (4), can be rewritten in a compact manner as:

$$\mathbf{t} = (\mathbf{I} - d\,\mathbf{P})\,\mathbf{K}[\![\mathbf{u}]\!] + f_d\,h_s\,\mathbf{t}_c \tag{22}$$

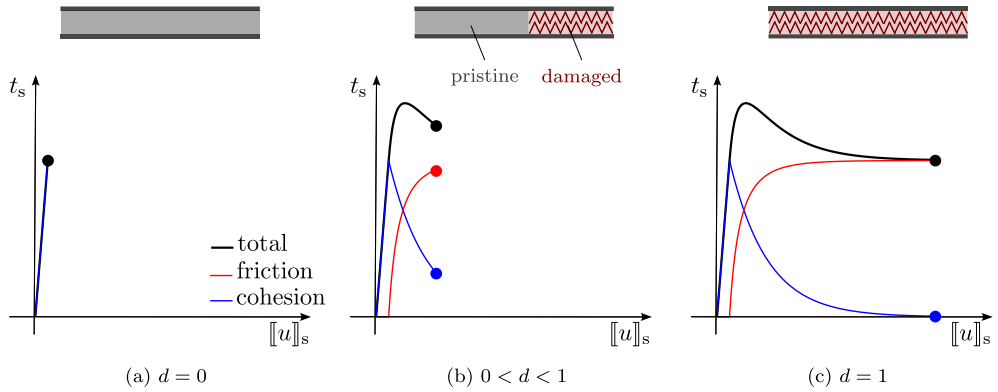


**Fig. 5.** Sketch of an interface damage state (*top*) and corresponding evolution of the cohesive-frictional response in compression-shear at constant compressive traction (*bottom*).

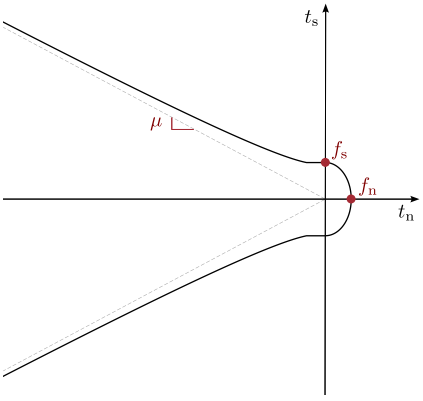


**Fig. 6.** Limit strength domain (solid line) and ultimate domain ($d \to 1$, dashed line).

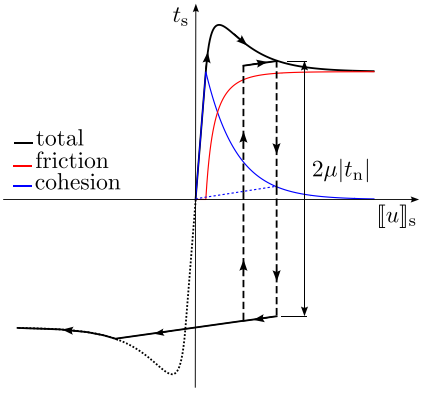


**Fig. 7.** Unloading-reloading behaviour for the mode II component of the response ($t_n < 0$).

where the Coulomb frictional term is collected in the vector $\mathbf{t}_c$:

$$\mathbf{t}_c = \mu\, k_n \langle -[\![u]\!]_n \rangle \left[0, 1\right]^T \tag{23}$$

The consistent tangent operator, which maps an increment in the displacement jump, $\delta[\![\mathbf{u}]\!]$, to an increment in the total traction, $\delta\mathbf{t}$, is given as:

$$\frac{\partial \mathbf{t}}{\partial [\![\mathbf{u}]\!]} = (\mathbf{I} - d\,\mathbf{P})\mathbf{K} - \mathbf{K}[\![\mathbf{u}]\!]\,\frac{\partial d^T}{\partial [\![\mathbf{u}]\!]} + h_s\,\mathbf{t}_c\,\frac{\partial f_d^T}{\partial [\![\mathbf{u}]\!]} + f_d\,\mathbf{t}_c\,\frac{\partial h_s^T}{\partial [\![\mathbf{u}]\!]} + f_d\,h_s\,\frac{\partial \mathbf{t}_c}{\partial [\![\mathbf{u}]\!]} \tag{24}$$

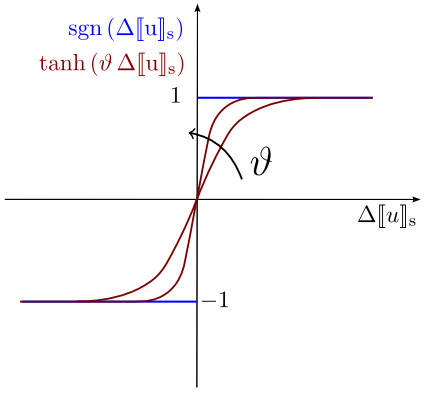


**Fig. 8.** Functions defining the frictional direction: discontinuous sign function (*in blue*) and smooth function $h_s$ for different values of the regularization parameter $\vartheta$ (*in red*). As the value of the regularization parameter $\vartheta$ increases, the smooth function approaches the discontinuous sign function.

The derivatives in this expression are derived in the following.

The derivative $\partial d/\partial [\![\mathbf{u}]\!]$, without damage accumulation ($d = d_0$) and during damage growth ($d > d_0$), is given as:

$$\frac{\partial d}{\partial [\![\mathbf{u}]\!]} = \begin{cases} \mathbf{0}_{2\times 1} & \text{if} \quad d = d_0 \\ \dfrac{\partial d}{\partial f_m}\dfrac{\partial f_m}{\partial [\![\mathbf{u}]\!]} + \dfrac{\partial d}{\partial k}\dfrac{\partial k}{\partial [\![\mathbf{u}]\!]} + \dfrac{\partial d}{\partial \phi}\dfrac{\partial \phi}{\partial [\![\mathbf{u}]\!]} + \dfrac{\partial d}{\partial [\![u]\!]_{eq}}\dfrac{\partial [\![u]\!]_{eq}}{\partial [\![\mathbf{u}]\!]} & \text{if} \quad d > d_0 \end{cases} \tag{25}$$

During damage growth, the derivatives of the damage parameter $d$ with respect to the mixed-mode quantities $f_m, k, \phi$ and $[\![u]\!]_{eq}$ at constant $[\![\mathbf{u}]\!]$ yield:

$$\frac{\partial d}{\partial f_m} = -\frac{\Gamma}{k^2\,[\![u]\!]_{eq}}\left(k + \phi\, f_m\right) \tag{26}$$

$$\frac{\partial d}{\partial k} = \frac{f_m\,\Gamma}{k^3\,[\![u]\!]_{eq}}\left(k + \phi\, f_m\right) \tag{27}$$

$$\frac{\partial d}{\partial \phi} = -\frac{f_m\,\Gamma}{k^2\,[\![u]\!]_{eq}}\left(f_m - k\,[\![u]\!]_{eq}\right) \tag{28}$$

$$\frac{\partial d}{\partial [\![u]\!]_{eq}} = \frac{f_m\,\Gamma}{k\,[\![u]\!]_{eq}^2}\left(1 + \phi\,[\![u]\!]_{eq}\right) \tag{29}$$

with

$$\Gamma = \exp\left[\phi\left(\frac{f_{\mathrm{m}}}{k} - [\![u]\!]_{\mathrm{eq}}\right)\right] \tag{30}$$

The derivatives of the mixed-mode quantities with respect to the displacement jump, $\partial f_{\mathrm{m}}/\partial[\![\mathbf{u}]\!]$, $\partial k/\partial[\![\mathbf{u}]\!]$, $\partial\phi/\partial[\![\mathbf{u}]\!]$ and $\partial[\![u]\!]_{\mathrm{eq}}/\partial[\![\mathbf{u}]\!]$, follow from applying the chain rule to each term. The term $\partial f_{\mathrm{m}}/\partial[\![\mathbf{u}]\!]$ reads:

$$\frac{\partial f_{\mathrm{m}}}{\partial[\![\mathbf{u}]\!]} = \frac{\partial f_{\mathrm{m}}}{\partial\beta}\frac{\partial\beta}{\partial[\![\mathbf{u}]\!]} \tag{31}$$

where

$$\frac{\partial f_{\mathrm{m}}}{\partial\beta} = \frac{1}{2}[\![u]\!]^{\mathrm{e}}_{\mathrm{n}}[\![u]\!]^{\mathrm{e}}_{\mathrm{s}}\sqrt{\frac{A}{B}}\times\left(\frac{\frac{\partial B}{\beta}}{\partial A} - \frac{B\frac{\partial A}{\partial\beta}}{A^2}\right) \tag{32}$$

with

$$A = \beta\left([\![u]\!]^{\mathrm{e}}_{\mathrm{n}}\right)^2 + (1-\beta)\left([\![u]\!]^{\mathrm{e}}_{\mathrm{s}}\right)^2 \tag{33}$$

$$B = (1-\beta)k_{\mathrm{n}}^2 + \beta\, k_{\mathrm{s}}^2 \tag{34}$$

$$\frac{\partial A}{\partial\beta} = \left([\![u]\!]^{\mathrm{e}}_{\mathrm{n}}\right)^2 - \left([\![u]\!]^{\mathrm{e}}_{\mathrm{s}}\right)^2 \tag{35}$$

$$\frac{\partial B}{\partial\beta} = -k_{\mathrm{n}}^2 + k_{\mathrm{s}}^2 \tag{36}$$

and

$$\frac{\partial\beta}{\partial[\![\mathbf{u}]\!]} = \begin{cases} \frac{2[\![u]\!]_{\mathrm{n}}[\![u]\!]_{\mathrm{s}}}{\left([\![u]\!]^2_{\mathrm{n}}+[\![u]\!]^2_{\mathrm{s}}\right)^2}\left[-[\![u]\!]_{\mathrm{s}},\ [\![u]\!]_{\mathrm{n}}\right]^{\mathrm{T}} & \text{if} \quad [\![u]\!]_{\mathrm{n}} > 0 \\ \mathbf{0}_{2\times1} & \text{if} \quad [\![u]\!]_{\mathrm{n}} \le 0 \end{cases} \tag{37}$$

The term $\partial k/\partial[\![\mathbf{u}]\!]$ is given as:

$$\frac{\partial k}{\partial[\![\mathbf{u}]\!]} = \frac{\partial k}{\partial f_{\mathrm{m}}}\frac{\partial f_{\mathrm{m}}}{\partial[\![\mathbf{u}]\!]} + \frac{\partial k}{\partial[\![u]\!]_{\mathrm{m}}}\frac{\partial[\![u]\!]_{\mathrm{m}}}{\partial[\![\mathbf{u}]\!]} \tag{38}$$

with

$$\frac{\partial k}{\partial f_{\mathrm{m}}} = \frac{1}{[\![u]\!]_{\mathrm{m}}} \tag{39}$$

$$\frac{\partial k}{\partial[\![u]\!]_{\mathrm{m}}} = -\frac{f_{\mathrm{m}}}{[\![u]\!]^2_{\mathrm{m}}} \tag{40}$$

$$\frac{\partial[\![u]\!]_{\mathrm{m}}}{\partial[\![\mathbf{u}]\!]} = \frac{\partial[\![u]\!]_{\mathrm{m}}}{\partial\beta}\frac{\partial\beta}{\partial[\![\mathbf{u}]\!]} \tag{41}$$

where

$$\frac{\partial[\![u]\!]_{\mathrm{m}}}{\partial\beta} = \frac{1}{2}[\![u]\!]^{\mathrm{e}}_{\mathrm{n}}[\![u]\!]^{\mathrm{e}}_{\mathrm{s}}\sqrt{A}\times\left(-\frac{\frac{\partial A}{\partial\beta}}{A^2}\right) \tag{42}$$

with $\partial\beta/\partial[\![\mathbf{u}]\!]$ already evaluated in Eq. (37). The derivative $\partial\phi/\partial[\![\mathbf{u}]\!]$ in Eq. (25) reads:

$$\frac{\partial\phi}{\partial[\![\mathbf{u}]\!]} = \frac{\partial\phi}{\partial k}\frac{\partial k}{\partial[\![\mathbf{u}]\!]} + \frac{\partial\phi}{\partial f_{\mathrm{m}}}\frac{\partial f_{\mathrm{m}}}{\partial[\![\mathbf{u}]\!]} + \frac{\partial\phi}{\partial G_{\mathrm{f,mix}}}\frac{\partial G_{\mathrm{f,mix}}}{\partial[\![\mathbf{u}]\!]} \tag{43}$$

where

$$\frac{\partial\phi}{\partial k} = \frac{2f_{\mathrm{m}}}{D^2}\left(D - 2k\,G_{\mathrm{f,mix}}\right) \tag{44}$$

$$\frac{\partial\phi}{\partial f_{\mathrm{m}}} = \frac{2k}{D^2}\left(D + 2f_{\mathrm{m}}^2\right) \tag{45}$$

$$\frac{\partial\phi}{\partial G_{\mathrm{f,mix}}} = -\frac{4\,k^2 f_{\mathrm{m}}}{D^2} \tag{46}$$

with

$$D = 2\,k\,G_{\mathrm{f,mix}} - f_{\mathrm{m}}^2 \tag{47}$$

and

$$\frac{\partial G_{\mathrm{f,mix}}}{\partial[\![\mathbf{u}]\!]} = \frac{\partial\psi_{\mathrm{I}}}{\partial\beta}\frac{\partial\beta}{\partial[\![\mathbf{u}]\!]}G_{\mathrm{f,I}} + \frac{\partial\psi_{\mathrm{II}}}{\partial\beta}\frac{\partial\beta}{\partial[\![\mathbf{u}]\!]}G_{\mathrm{f,II}} \tag{48}$$

with

$$\frac{\partial\psi_{\mathrm{I}}}{\partial\beta} = -\frac{([\![u]\!]^{\mathrm{e}}_{\mathrm{n}})^2([\![u]\!]^{\mathrm{e}}_{\mathrm{s}})^2}{A^2} \tag{49}$$

$$\frac{\partial\psi_{\mathrm{II}}}{\partial\beta} = \frac{([\![u]\!]^{\mathrm{e}}_{\mathrm{n}})^2([\![u]\!]^{\mathrm{e}}_{\mathrm{s}})^2}{A^2} \tag{50}$$

The last derivative in Eq. (25) reads:

$$\frac{\partial[\![u]\!]_{\mathrm{eq}}}{\partial[\![\mathbf{u}]\!]} = \frac{1}{[\![u]\!]_{\mathrm{eq}}}\left[\langle[\![u]\!]_{\mathrm{n}}\rangle,\ [\![u]\!]_{\mathrm{s}}\right]^{\mathrm{T}} \tag{51}$$

Finally, the derivatives pertaining to the frictional contribution (last three terms in Eq. 24) are given as:

$$\frac{\partial f_{\mathrm{d}}}{\partial[\![\mathbf{u}]\!]} = p\,d^{p-1}\frac{\partial d}{\partial[\![\mathbf{u}]\!]} \tag{52}$$

$$\frac{\partial h_{\mathrm{s}}}{\partial[\![\mathbf{u}]\!]} = \left[1 - \tanh^2\left(\vartheta\,\Delta[\![u]\!]_{\mathrm{s}}\right)\right]\left[0,\vartheta\right]^{\mathrm{T}} \tag{53}$$

$$\frac{\partial\mathbf{t}_{\mathrm{c}}}{\partial[\![\mathbf{u}]\!]} = \mu\,k_{\mathrm{n}}\begin{bmatrix} 0 & 0 \\ \frac{\langle-[\![u]\!]_{\mathrm{n}}\rangle}{|[\![u]\!]_{\mathrm{n}}|} & 0 \end{bmatrix} \tag{54}$$

## 3. Validation against a masonry shear wall with an opening

In this section, the improved material model is applied to simulate the response of a masonry shear wall subjected to compression-shear loading [42,43] through a simplified micromodelling approach. First, a preliminary numerical study of the shear wall under monotonic action is carried out to investigate the sensitivity of the response to different values of the regularization parameter $\vartheta$, Eq. (20). Subsequently, the model is validated against the cyclic laboratory test of the shear wall [42,43]. Finally, the effects of varying the value of the coupling parameter $p$, Eq. (19), and the quality of the head-joints on the response are investigated.

### 3.1. Experimental test and numerical model

The experimental setup of the shear wall under compression-shear loading [42,43] is shown in Fig. 9. The specimen is made of clay bricks, $210\times50$ mm$^2$, laid in a running bond configuration, with a mortar joint thickness of 10 mm. The thickness of the wall is 100 mm. It is placed on a fully constrained steel beam (HEA300) and it is restrained at the top by another steel beam (HEA600) which can vertically translate and rotate during the test. A concrete lintel is located above an asymmetric opening and two notches are inserted during the construction of the specimen. The wall is subjected to a (constant) vertical overload of 0.12 MPa, before a horizontal quasi-static cyclic displacement $u$ is applied to the top beam.

**Table 1**
Shear wall: material parameters.

| | Bricks | Lintel | | Bed-joint interfaces | | |
|---|---|---|---|---|---|---|
| $E$ [N mm$^{-2}$] | 8000 | 31,000 | [42,43] | $k_n$ [N mm$^{-3}$] | 115 | [44] |
| $\nu$ | 0.14 | 0.2 | [42,43] | $k_s$ [N mm$^{-3}$] | 50 | [44] |
| $\rho$ [kg m$^{-3}$] | 1708 | 2400 | [42,43] | $f_n$ [N mm$^{-2}$] | 0.09 | [42,43] |
| | | | | $f_s$ [N mm$^{-2}$] | 0.14 | [42,43] |
| | | | | $G_{f,I}$ [N mm$^{-1}$] | 0.014 | [45,46] |
| | | | | $G_{f,II}$ [N mm$^{-1}$] | 0.14 | [45,46] |
| | | | | $\alpha$ | 1 | [47] |
| | | | | $\mu$ | 0.79 | [42,43] |
| | | | | $p$ | 3 | [·] |
| | | | | $\vartheta$ | $10^5$ | [·] |

[42,43] material characterization; [44] formula; [45,46] formula; [47] formula; [·] calibration.

In the numerical model, bricks, lintel and beams are modelled with bilinear elastic elements. The only source of nonlinearity is provided by the nonlinear zero-thickness interfaces located between the expanded bricks, according to the simplified micromodelling approach, Fig. 1. The material parameters of bricks, lintel and bed-joints used in the simulations are summarized in Table 1. The interface stiffness is computed as [44]:

$$k_n = \frac{E_b\, E_m}{h_m\left(E_b\, E_m\right)}, \quad k_s = \frac{G_b\, G_m}{h_m\left(G_b\, G_m\right)} \tag{55}$$

where the subscripts b and m refer to brick and mortar, respectively; $E$ and $G$ are the elastic moduli and $h_m$ is the mortar thickness. These relations do not result in penalty stiffness values. Therefore, in the compressive areas, exaggerated deformed plots may show penetration of the interface faces. However, this should be interpreted as the actual compression of the mortar joints that are not explicitly modelled. The interface fracture energies are determined by the formulas [45,46]:

$$G_{f,I} = 0.16\, f_n, \quad G_{f,II} = 10\, G_{f,I} \tag{56}$$

Due to the construction process, the head-joints are usually characterized by poorer mechanical properties than the bed-joints. To account for this, their material parameters are evaluated from those of the bed-joints by applying a reduction of 15%. The effect of this assumption on the response is explored later in this section.

In all simulations, continuum elements (masonry units, lintels and beams belonging to the experimental setup) are modelled by 4-node plane stress finite elements with 2×2 Gauss integration, whereas 4-node zero-thickness finite elements with Lobatto integration are used for the interfaces [48,49]. The total number of interface elements is 2716. The analyses are performed with adaptive stepping and Newton-Raphson with force norm of $10^4$ or an energy norm of $10^5$.

### 3.2. Performance assessment of the frictional regularization parameter

The performance of the proposed formulation and the effect of varying the new model parameter, $\vartheta$, are investigated by simulating the shear wall subjected to a monotonic horizontal displacement of the top edge (Fig. 9).

A comparison between the global response curves, expressed in terms of total horizontal reaction $F_h$ with respect to the horizontal displacement of the top left corner $u_P$, obtained without and with regularization of the frictional term, is carried out and presented in Fig. 10(a). The function used to determine the direction of the friction is specified in Fig. 10(b). To highlight the effect of the frictional contribution, the response of a purely cohesive material (without friction) is shown as reference line (brown solid curve). For this case, the softening branch in the global response indicates damage localization in a horizontal mortar layer, resulting in a sliding plane at the base of a pier and a subsequent reduction of the capacity. The response obtained without regularization of the frictional term is depicted in dark blue. It can be observed that determining the direction of $\mathbf{t}_{fric}$, Eq. (4), through the discontinuous function, $\mathrm{sgn}\left(\Delta[\![u]\!]_s\right)$, leads to premature abortion of the analysis, indicated with a dark blue cross. In contrast, the use of the smooth function, $h_s$, allows for simulating the complete response without convergence issues for a wide range of values of the regularization parameter $\vartheta$. However, the capacity of the wall increases with $\vartheta$ since, to properly model the frictional contribution, the absolute value of $h_s$ should approximate unity ($|h_s| \approx 1$). Fig. 11 illustrates the frictional contribution to the traction, $d^p h_s \mu \langle -t_n \rangle$, at $u_P = 1.5$ mm for analyses with $\vartheta$-values of $10^3$, $10^5$ and $10^6$. It can been seen that for $\vartheta = 10^3$ the frictional response arises in a smaller portion of the wall than for $\vartheta = 10^5$ (*cf.* Fig. 11a and b). This is due to the fact that for low values of $\vartheta$, in some areas of the structure $|h_s| < 1$, and as a consequence the friction is not entirely accounted for. It is worth noting that when the value of $\vartheta$ is considerably small (dashed pink line), the corresponding global response approaches the curve obtained without friction. As $\vartheta$ increases, $|h_s|$ reaches unity in more points and consequently the frictional contribution grows (*cf.* Fig. 11a and b) together with capacity (*cf.* the dotted gray and purple curves in Fig. 10(a). When the friction is sufficiently accounted for, a further increment of $\vartheta$ does not change the frictional response (*cf.* Fig. 11b and c) and, therefore, does not result in an increase of capacity (the orange and purple curves overlap, Fig. 10(a). However, upon further increasing $\vartheta$, convergence issues re-emerge since $h_s$ approaches $\mathrm{sign}(\Delta[\![u]\!]_s)$ as $\vartheta \to \infty$, Eq. (21). Consequently, the smooth function $h_s$ is so steep that it is almost characterized by an unbounded tangent for $\Delta[\![u]\!]_s = 0$, (cyan line, Fig. 10). It is worth noting that this numerical problem arises for a value of $\vartheta$ three orders of magnitude higher than what already represents a good approximation for the sign function (purple line, Fig. 10).

From this analysis, it can be concluded that an optimum for $\vartheta$ can be found for which the response does not change with further increase, while improving the robustness of the simulations.

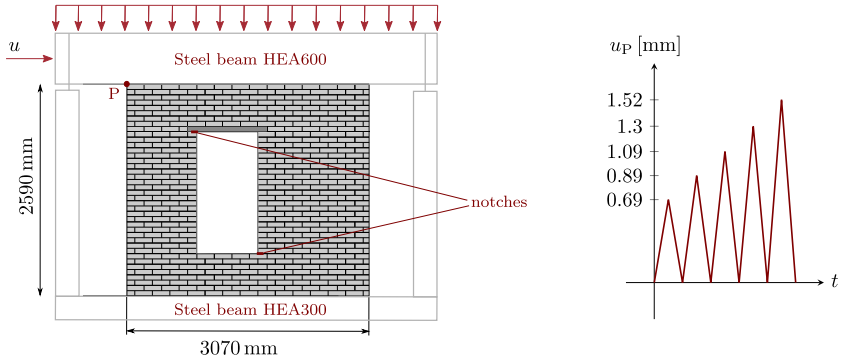


**Fig. 9.** Experimental setup (adapted from [42]) and cyclic loading scheme. The analysis is quasi-static. The variable $t$ on the $x$-axis indicates a pseudo-time.

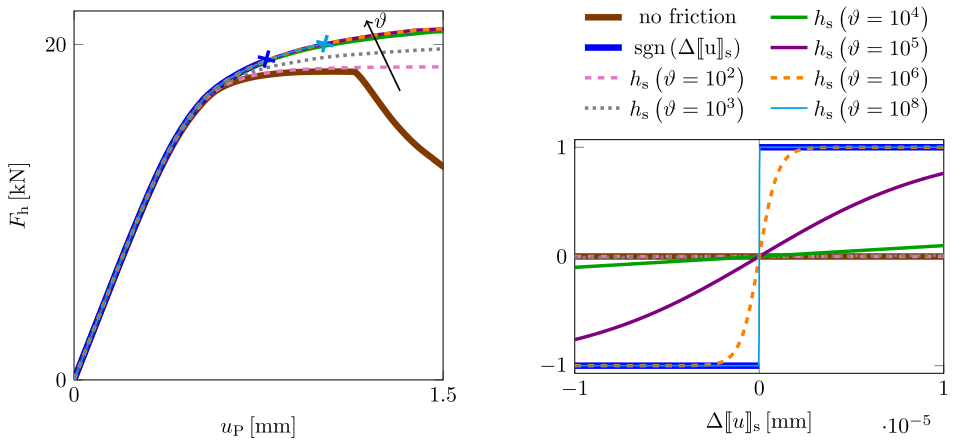


(a) Global force-displacement curves, the loss of convergence of the analysis is indicated by a cross

(b) Function used to identify the direction of the frictional contribution. For low values of $\vartheta$, the smooth function $h_s$ (Eq. (20)) is so shallow that it appears almost as a horizontal line in the depicted range of $\Delta[\![u]\!]_s$-values

**Fig. 10.** Sensitivity analysis varying the values of the regularization parameter $\vartheta$.

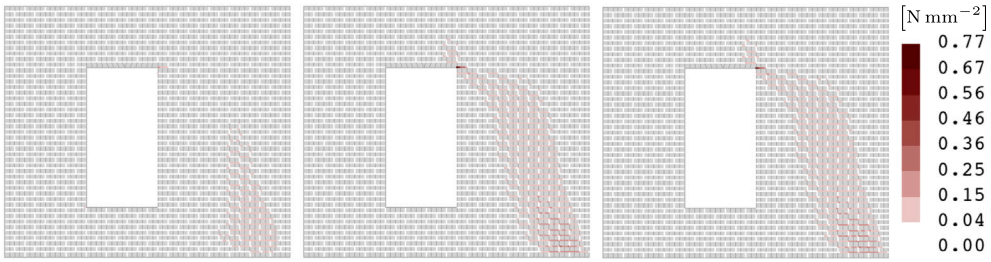


(a) $\vartheta = 10^3$ (b) $\vartheta = 10^5$ (c) $\vartheta = 10^6$

**Fig. 11.** Frictional contribution to the traction, $d^p h_s \mu \langle -t_n \rangle$, at the last stage of the monotonic analysis ($u_P = 1.5$ mm) for different values of the regularization parameter $\vartheta$.

### 3.3. Simulation of the experimental cyclic test

After having demonstrated the effect of varying the regularization parameter $\vartheta$ through a monotonic test of the shear wall, the model is validated against the laboratory test of the same shear wall subjected to a cyclic horizontal displacement of the top beam. During the experiment, each displacement amplitude is applied ten times before being progressively increased. To save computational time, only one cycle for each amplitude is numerically simulated (Fig. 9 *right*). For the cyclic analysis, the regularization parameter $\vartheta$ is set to $10^5$, as indicated by the previous numerical study (Section 3.2).

Experimental and numerical global response curves are compared in Fig. 12(a). The numerical model satisfactorily captures the initial stiffness, the capacity, the energy dissipated during the analysis and the unloading-reloading behaviour of the wall. The hysteresis loops in the global response curve emerge naturally from the decomposition of the total traction into cohesive and frictional parts, with the former characterized by a secant unloading and the latter by a rigid unloading. In addition, the crack pattern at the maximum applied displacement, $u_P = 1.52$ mm, is in good agreement with the experiment (*cf.* Fig. 12b and c). It can be observed that the location of the cracks is well reproduced, although their widths are slightly underestimated and a small mismatch with respect to the direction of the bottom right crack can be noticed.

A mesh refinement study is carried out: two mesh sizes are used, a coarser and a finer mesh. In case of brickwork masonry characterized by strong bricks and weak mortar joints [12], a refinement of the mesh does not modify the potential crack path which remains constrained in the joint layers. The comparison between the global response curves (Fig. 13a) and the crack patterns (*cf.* Fig. 13b and c) shows that the model is mesh-insensitive. A more accurate representation of the evolution of the crack pattern together with an objective description of the energy dissipated during the analysis of strain softening materials with respect to the mesh size [13] represents considerable advantages of discrete over local continuum models [21]. The drawback of micromodels is that they usually require higher computational cost and longer pre-processing times. In particular, the pre-processing phase can become tedious when larger structures and complex bond patterns are considered. Nonetheless, it is important to highlight that the model with consistent tangent is rather efficient and the coarse-mesh simulation takes 25 min on a laptop computer with processor 12th Gen Intel(R) Core(TM) i7-1265U 1.80 GHz and RAM 16 GB (CPU time: 1519 s).

### 3.4. Sensitivity studies on model parameters affecting the frictional contribution

In the following, the influence on the response of the model parameters $p$ and $\vartheta$ (Eqs. 19 and 20) that affect the frictional term is explored.

First, the effect of varying the coupling parameter $p$, which determines the interaction between cohesive and frictional behaviours, is investigated. Increasing $p$ results in a delay in the mobilization of the

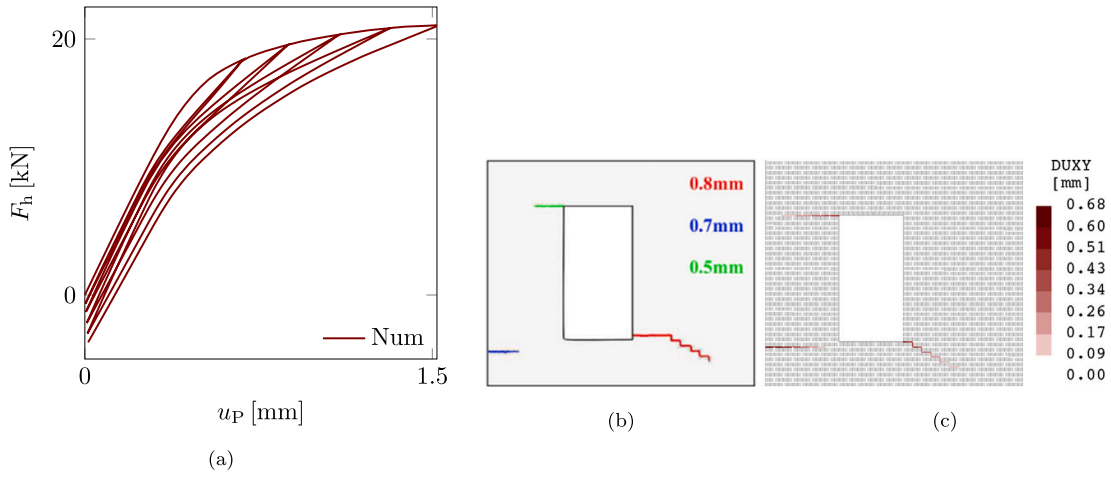


**Fig. 12.** Experimental vs numerical response of the shear wall under cyclic loading: global response curves (a); experimental crack width from [42] (b) and numerical crack width (c) at the maximum applied displacement $u_P = 1.52$ mm.

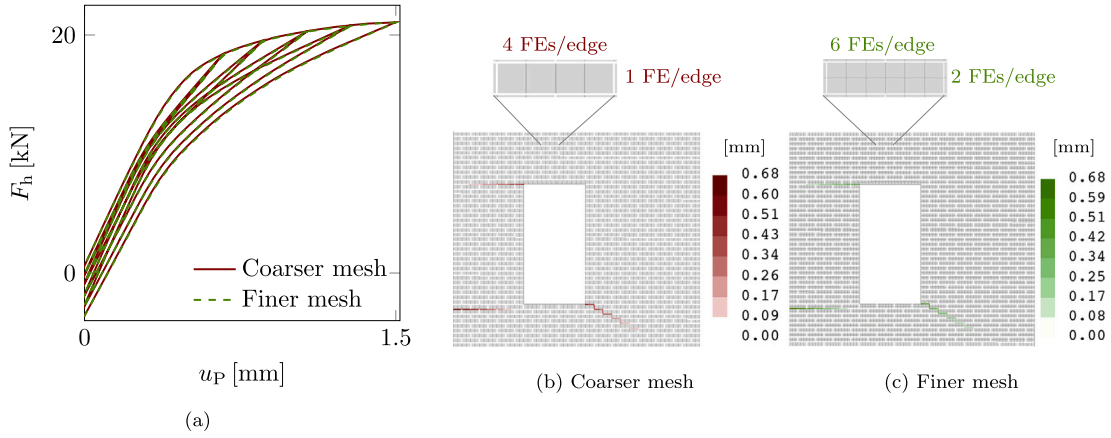


**Fig. 13.** Mesh refinement study: global response curves (a); numerical crack width with different mesh sizes at the maximum applied displacement $u_P = 1.52$ mm (b) and (c).

frictional term, since a higher level of damage is required to attain the same contribution of the friction (Fig. 14a). This results in a lower capacity at the integration point level: the strength of the material decreases (Fig. 14b) and the limit strength domain reduces (Fig. 14c). This ultimately leads to a lower capacity of the wall (Fig. 14d). Moreover, as the value of $p$ grows, the frictional contribution reduces (Fig. 15), influencing the amount of permanent displacements accumulated in the system and therefore affecting the cyclic response. Since the cohesive part of the response is characterized by secant unloading (no residual displacements upon unloading) whereas the frictional part is characterized by rigid unloading (no recovery in displacements upon unloading), it can be observed that the force $F_h$ at the end of the analysis, $u_P = 0$ mm, changes with $p$ (from the value −3.6 to -3.0 kN by assuming, respectively, $p = 3$ and $p = 30$, Fig. 14d).

Next, a sensitivity study with different values of the regularization parameter $\vartheta$ is illustrated in Fig. 16. It can be observed that, similarly to the monotonic case (Section 3.2), when a cyclic load is applied, the global response curves obtained with sufficiently high values of the regularization parameter, $\vartheta = 10^5$ and $10^6$, overlap (Fig. 16a). The corresponding friction contour plots at the maximum applied displacement ($u_P = 1.52$ mm) show complete agreement (*cf.* Fig. 15a and 16b). Therefore, as already explored with the monotonic analysis in Section 3.2, by using $\vartheta = 10^5$, the smooth function $h_s$ represents a good approximation for the sign function, Eq. (20), and the frictional part of the traction is adequately taken into account.

### 3.5. Head-joints sensitivity

So far, the analyses were performed with a 15% reduction of the head-joint parameters with respect to the bed-joint values. To explore the effect on the response of the head-joint quality, which can vary depending on the manufacturing process [50], a sensitivity study with different values of the head-joints material parameters is carried out. The properties are chosen as 100%, 85% (used in the previous analyses) and 50% of the corresponding bed-joints values (Table 2). The outcomes of the simulations are compared in terms of global response curves and crack patterns.

The global response curve (Fig. 17a) is only slightly affected by a variation in the head-joint properties, indicating that the test is governed mainly by the bed-joints characteristics. If 100% or 85% of the bed-joint properties are used to characterize the head-joints, the outcome of the simulation does not change, neither in terms of global response (blue and red curves, Fig. 17a) nor crack pattern (*cf.* Fig. 12c and Fig. 17b). The only difference concerns the bottom left crack that develops in a different mortar layer. In contrast, some discrepancies in the results

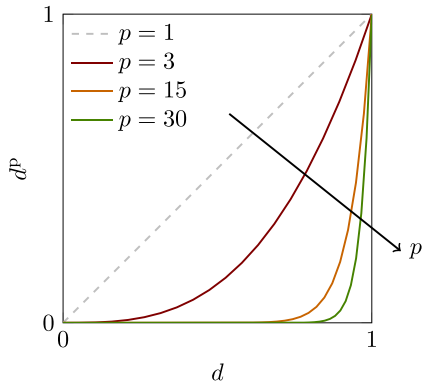


(a) Function governing the combination between cohesion and friction (Eq. (19))

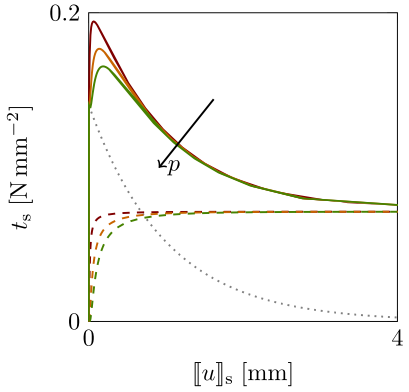


(b) Bed-joint mode II component of the response: total traction (solid line), cohesion (dotted), friction displayed for $t_n = \text{const} < 0$ (dashed)

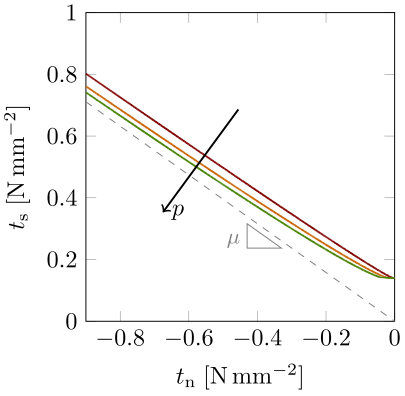


(c) Bed-joint limit strength domain (solid line), ultimate domain ($d \to 1$, dashed line), Figure 6

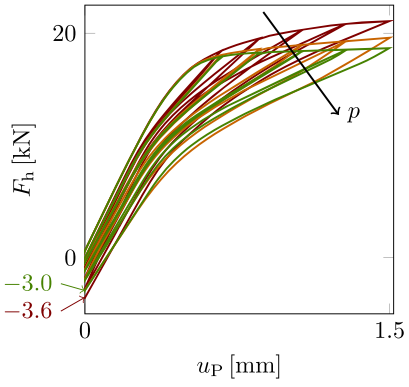


(d) Global response curves

**Fig. 14.** Sensitivity analysis varying $p$.

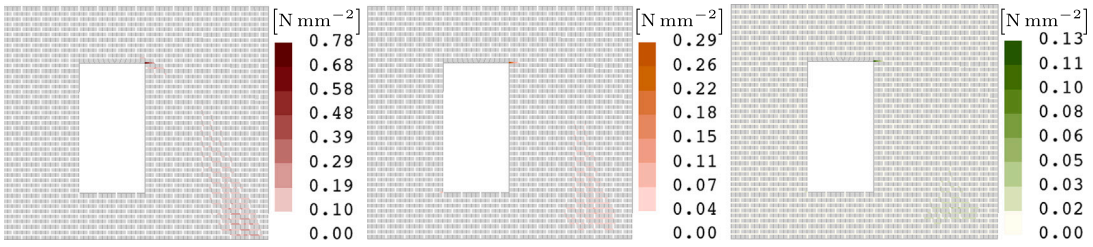


(a) $p = 3$ (b) $p = 15$ (c) $p = 30$

**Fig. 15.** Frictional contribution to the traction, $d^p h_s \, \mu \langle -t_n \rangle$, at the maximum applied displacement $u_P = 1.52$ mm for different values of the coupling parameter $p$ and with regularization parameter $\vartheta = 10^5$.

**Table 2**
Shear wall: head-joint material parameters as percentages of the bed-joint values.

| | 100% | 85% | 50% | |
|---|---|---|---|---|
| $k_n$ | 115 | 100 | 55 | N mm$^{-3}$ |
| $k_s$ | 50 | 40 | 25 | N mm$^{-3}$ |
| $f_n$ | 0.09 | 0.075 | 0.045 | N mm$^{-2}$ |
| $f_s$ | 0.14 | 0.12 | 0.07 | N mm$^{-2}$ |
| $G_{f,I}$ | 0.014 | 0.012 | 0.007 | N mm$^{-1}$ |
| $G_{f,II}$ | 0.14 | 0.12 | 0.07 | N mm$^{-1}$ |
| $\alpha$ | 1 | 1 | 1 | |
| $\mu$ | 0.79 | 0.67 | 0.4 | |
| $p$ | 3 | 3 | 3 | |
| $\vartheta$ | $10^5$ | $10^5$ | $10^5$ | |

can be observed when a reduction of 50% of the head-joint parameters is applied. This case shows a slightly higher capacity (green curve, Fig. 17a) and a crack pattern that differs from the other simulations: at the top left, a crack grows diagonally and at the bottom left, a crack localizes in two mortar layers, (*cf.* Fig. 12c, 17b and c). This crack pattern requires more energy to develop. Therefore, although in this case poorer properties are used for characterizing the head-joints, the energy dissipated to meet the same demand in displacement is higher, explaining the increased capacity. However, since the specimen is built in a laboratory and particular attention is paid to its construction, a large reduction in the head-joint properties with respect to the bed-joints does not appear appropriate. Thus, the head-joints material parameters were assumed as 85% of the bed-joints values as base case throughout this section.

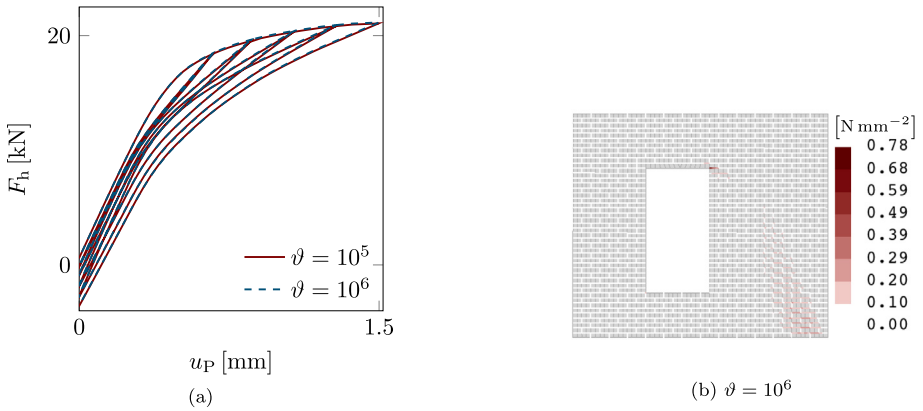


**Fig. 16.** Sensitivity analysis of the regularization parameter $\vartheta$: global response curves (a); frictional contribution to the traction, $d^p h_s \mu \langle -t_n \rangle$, at the maximum applied displacement $u_P = 1.52$ mm for $\vartheta = 10^6$ (b).

### 3.6. Discussion

In this section, the performance of the interface material model has been examined. First, the effect of regularizing the frictional term on the response has been investigated for a monotonic loading case and a procedure to achieve objectivity of the frictional contribution has been outlined. Subsequently, the model has been used to simulate a cyclic experimental test. The results of the simulation show that the numerical model is able to accurately capture capacity, stiffness degradation and energy dissipated during the cycles and describe the complex unloading-reloading behaviour characteristic of masonry. Furthermore, the crack pattern is well reproduced and the model is mesh-objective. The effect of varying the model parameter that governs the interaction between cohesion and friction has been investigated and its influence on the response has been discussed. Moreover, sensitivity analyses varying the value of the regularization parameter confirm the objectivity of the response during the cyclic simulation. For both the monotonic and cyclic tests, a $\vartheta$-value of $10^5$ appears appropriate. However, this may vary depending on the specific case. Therefore, varying $\vartheta$ is recommended to assess the objectivity of the response and the robustness of the simulation. Finally, the sensitivity study of the head-joint material parameter shows that, in this case study, the quality of the head-joints has minor influence on the response.

The outcomes of the simulations in this section demonstrate that the removal of the loading-unloading discontinuity in the Coulomb frictional term and the derivation of the consistent tangent stiffness matrix lead to an efficient and robust formulation. Objective results are achieved and the frictional term is adequately described.

## 4. Validation against a masonry spandrel wall

In this section a full-scale spandrel test subjected to cyclic settlements [51,52] is simulated to assess the performance of the model under complex loading schemes and damage patterns. Furthermore, the effects on the response of varying the regularization parameter $\vartheta$ and using different values of the material properties are investigated.

### 4.1. Experimental test and numerical model

The spandrel wall [51,53] is made of clay bricks, with dimensions $250 \times 120 \times 60$ mm$^3$, laid in a double-wythe English bond pattern. It consists of a spandrel, placed on a timber lintel, and two piers, see Fig. 18. The piers are located on lever beams which rotate, alternatively, clockwise and anticlockwise with increasing amplitude. Additional loads are applied to the specimen via vertical and horizontal tendons. Specifically, a vertical stress $\sigma_v$ is imposed on each pier and a horizontal load $H_{sp}$ is applied to the spandrel. The magnitude of these loads is modified three times during the experimental test to arrest the development of failure mechanisms outside the spandrel. This resulted in the sequential application of three combinations of loads, corresponding to three loading phases (LP), shown in Table 3.

The test is simulated through a two-dimensional finite element model, consequently the actual geometry in the thickness is neglected.

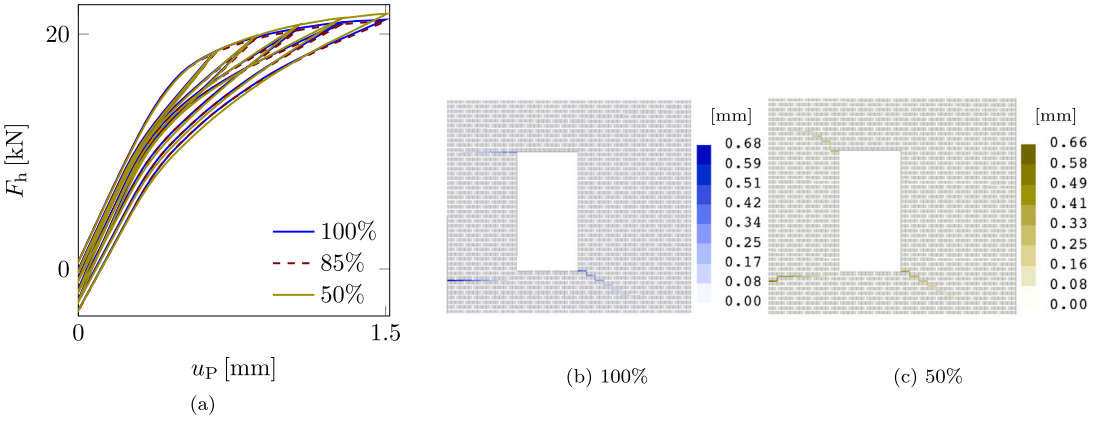


**Fig. 17.** Sensitivity analysis for different reductions of head-joint parameters with respect to the corresponding bed-joints values: global response curves (a); crack width at the maximum applied displacement $u_P = 1.52$ mm (b), (c).

**Table 3**
Spandrel test: loads in the tendons during each loading phase.

| | $\sigma_v$ [N mm$^{-2}$] | $H_{sp}$ [kN] |
|---|---|---|
| LP 1 | 0.18 | 80 |
| LP 2 | 0.33 | 80 |
| LP 3 | 0.33 | 40 |

Before the experimental test started, a crack above the lintel was recorded, thus, in the numerical model, the corresponding interfaces are assumed to be pre-damaged (Fig. 18). The material parameters used in the analysis are summarized in Table 4. For the bed-joint interfaces, the parameters $k_n, k_s, G_{f,I}, G_{f,II}$ are computed through Eqs. (55) and (56). The interface strength in mode I, $f_n$, is evaluated as [44]:

$$f_n = \frac{f_s}{2\mu} \tag{57}$$

The head-joint properties are assumed as 85% of the bed-joint values to account for their inherently lower quality and the simplified geometry. Moreover, the friction coefficient acting between the wooden lintel and clay bricks is assumed to be 0.6 [54,55]. The use of parameters from material characterization or formulas revealed a significant discrepancy between the experimental and numerical initial stiffness of the spandrel. Therefore, the value of the elastic stiffness of the bricks $E_b$ has been reduced to match the initial slope of the experimental response curve. To investigate the consequences of this choice, a sensitivity study varying the value of $E_b$ is carried out later in this section.

Experimental and numerical outcomes are compared in terms of global response curves and evolution of the crack pattern. The global response curve is expressed as the shear force in the spandrel $V$ with respect to the rotation of the piers $\varphi_p$. These quantities are computed as the average of the southern and northern values (see Fig. 18), indicated by the subscripts S and N, respectively. The shear forces $V_{S/N}$ are evaluated as:

$$V_{S/N} = F_{act,S/N} + R_{sup,S/N} - \frac{W}{2} \tag{58}$$

where $F_{act,S/N}$ is the force in the actuators, $R_{sup,S/N}$ is the vertical reaction of the supports and $W$ is the self-weight of the complete set-up. The half-amplitude of the rotations (positive if clockwise, negative otherwise) is computed as:

$$\varphi_{p,S/N} = \frac{v_{1,S/N} - v_{2,S/N}}{l_{pier}} \tag{59}$$

where $v_{i,S/N}$, $i = 1,2$ indicates the vertical displacement of the points $P_{1,S/N}$ and $P_{2,S/N}$ and $l_{pier} = \overline{P_{1,S/N}P_{2,S/N}}$ is the length of the piers (Fig. 18).

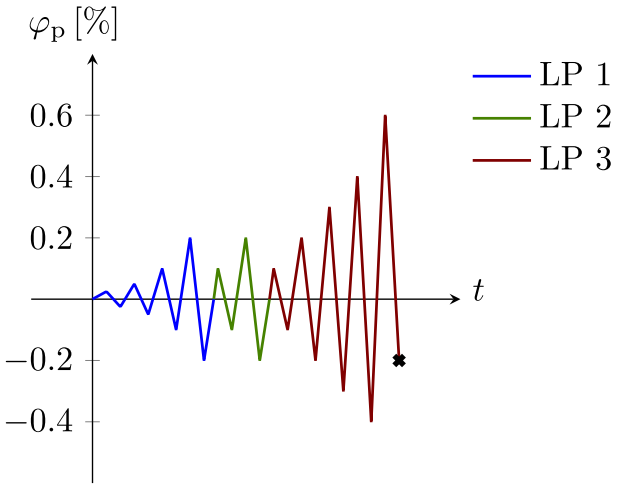


**Fig. 19.** Cyclic loading scheme. The cross indicates the end of the simulation.

During the experiment, the magnitude of the rotations is increased every two cycles. To reduce the computational cost, only one cycle for each amplitude is numerically simulated. The loading scheme is illustrated in Fig. 19.

In all simulations, continuum elements (masonry units, lintels and beams belonging to the experimental setup) are modelled by 4-node plane stress finite elements with 2×2 Gauss integration, whereas 4-node zero-thickness finite elements with Lobatto integration are used for the interfaces [48,49]. The total number of interface elements is 3147. The load step sizes are automatically adjusted with adaptive stepping.

### 4.2. Simulation of experimental cyclic test

Experimental and numerical outcomes are compared in Fig. 20 and Fig. 22. For the first loading phase LP 1, both the global response (Fig. 20a) and the crack pattern (*cf.* Fig. 21a–d) are in good correspondence with the experiment. For the second loading phase LP 2, the capacity is well captured, although the hysteresis loop is underestimated (Fig. 20b). In the piers, the horizontal cracks that occur during the previous loading phase (LP 1, Fig. 21d), re-open during the second loading phase LP 2, without dissipating further energy. Nevertheless, the evolution of the crack pattern is adequately described (Fig. 21e–h). During the third loading phase LP 3, numerical and experimental responses are in good agreement until $\varphi_p = 0.2\%$ and the capacity is well captured (Fig. 20c). Furthermore, experimental and numerical crack patterns show a good match, with the formation of vertical cracks with different lengths at the edges of the spandrel (*cf.* Fig. 22a and b). These

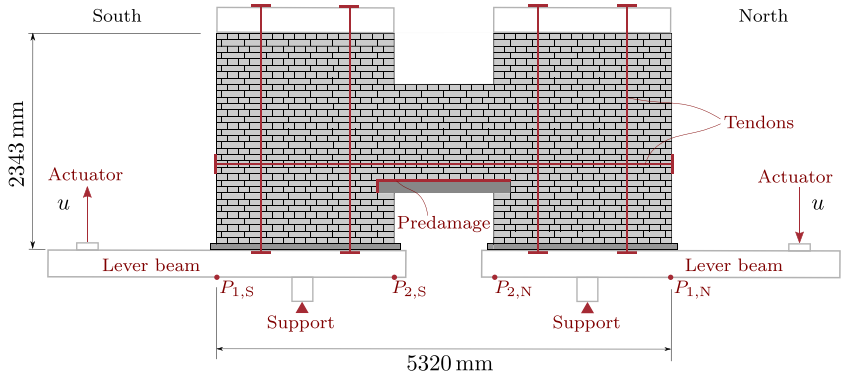


**Fig. 18.** Spandrel TUA: experimental setup.

**Table 4**
Spandrel test: material parameters.

| | Bricks | | Lintel | | | Bed-joint | | Head-joint [·] |
|---|---|---|---|---|---|---|---|---|
| $E$ [N mm$^{-2}$] | 1000 | [·] | 6700 | [51,52] | $k_n$ [N mm$^{-3}$] | 200 | [44] | 170 |
| $\nu$ | 0.15 | [51,52] | 0.3 | [51,52] | $k_s$ [N mm$^{-3}$] | 80 | [44] | 68 |
| $\rho$ [kg m$^{-3}$] | 1880 | [51,52] | 477 | [51,52] | $f_n$ [N mm$^{-2}$] | 0.2 | [44] | 0.17 |
| | | | | | $f_s$ [N mm$^{-2}$] | 0.35 | [51,52] | 0.3 |
| | | | | | $G_{f,I}$ [N mm$^{-1}$] | 0.03 | [45,46] | 0.025 |
| | | | | | $G_{f,II}$ [N mm$^{-1}$] | 0.3 | [45,46] | 0.25 |
| | | | | | $\alpha$ | 1 | [47] | 1 |
| | | | | | $\mu$ | 0.85 | [51,52] | 0.72 |
| | | | | | $p$ | 1 | [·] | 1 |
| | | | | | $\vartheta$ | $2 \cdot 10^4$ | [·] | $2 \cdot 10^4$ |

[51,52] material characterization; [44] formula; [45,46] formula; [47] formula; [·] calibration

cracks are caused by the asymmetric application of the loading amplitudes which are gradually increased. Discrepancies in the results arise at $\varphi_p = -0.2\%$ when, in the experimental test, a loss of capacity due to the occurrence of a diagonal shear crack in the spandrel is observed (Fig. 20c and 22c). Conversely, in the numerical simulation, this diagonal shear crack does not develop (Fig. 22d), leading to an overestimation of the global response curve (Fig. 20c). As the analysis progresses, the damage continues to evolve and the two vertical cracks at the edges of the spandrel grow towards the lintel (Fig. 22d and f). At $\varphi_p = 0.4\%$ an area of diffuse damage at the base of the spandrel is visible (Fig. 22f). At $\varphi_p = -0.4\%$, the two vertical cracks at the edges of the spandrel reach the lintel (Fig. 22h). When the rotation of the beams reaches the value $\varphi_p = 0.6\%$, in the simulation, a crack initiates at the left edge of the spandrel, while another crack, starting at the right side, reaches the top (Fig. 22j). The simulation was terminated at $\varphi_p = -0.2\%$ when these two cracks merge (Fig. 22k).

Finally, in Fig. 20(c) in both the experimental and numerical global response curves, from $\varphi_p = 0.6\%$ to the end of the simulation (indicated by a cross), a change in curvature can be noticed. This recovery in stiffness is due to the re-closure of the vertical cracks at the edges of the spandrel (Fig. 22j).

### 4.3. Sensitivity analysis varying $\vartheta$

In the following, the effect of varying the value of the regularization parameter $\vartheta$ is explored. Fig. 23 shows the first cycles of the global response curves (LP 1) for different values of the model parameter $\vartheta$. It can be observed that the curves obtained with $\vartheta = 2 \cdot 10^4$ and $\vartheta = 1 \cdot 10^5$ overlap (red and green curves). The parameter $\vartheta = 2 \cdot 10^4$ (Table 4) is sufficiently high to represent a good approximation of the discontinuous sign function and, therefore, adequately describes the frictional term. When the value of this regularization parameter is considerably increased, $\vartheta = 1 \cdot 10^6$ (orange curve), convergence problems reappear and the analysis stops prematurely (orange cross in the global response curve). Therefore, without the regularization of the frictional term, an implicit analysis of the spandrel test was not possible. The use of a smooth approximation of the sign function results in robust analysis, without compromising accuracy.

### 4.4. Sensitivity analysis varying $E_b$

As mentioned in Section 4.1, the use of parameters from material characterization leads to a mismatch between the experimental and numerical initial stiffness of the spandrel. Fig. 24 shows the first cycles of the global response curve (LP 1) obtained by using the material parameters from Table 4, and varying the Young modulus of the bricks, $E_b$. Assuming the value of $E_b$ from material characterization results in an overestimation of the initial slope (blue curve). Therefore, the value of the elastic modulus of the bricks has been reduced to match the initial stiffness of the system (red curve) and has been used throughout Section 4. Nevertheless, this choice affects the results of the simulation: the energy dissipated by the system diminishes, since part of the displacement demand is accommodated by the brick elastic deformations which increase as the value of $E_b$ decreases. The present analysis confirms that a reduced value of the Young modulus of the bricks is necessary for capturing the initial stiffness of the spandrel, as done throughout Section 4.

### 4.5. Discussion

In this section, the interface material model has been tested by simulating a spandrel wall subjected to differential settlements. The outcome of the simulation is in good agreement with the experiment for the loading phases LP 1 and LP 2, both in terms of global response curves and crack patterns. For the loading phase LP 3, a mismatch between numerical and experimental outcomes has been observed: the simulation is unable to predict the formation of a shear crack in the spandrel, leading to a discrepancy in the global response. However, it is important to highlight that the interface material parameters are taken from material characterization or formulas when experimental data is unavailable, without further calibration. Moreover, by considering the 2D simplification of the complex geometry, the assumptions about the brick stiffness and the experimental uncertainties regarding boundary conditions and material characterization, the numerical model decently describes the evolution of the crack pattern.

The sensitivity study of the regularization parameter $\vartheta$ has demonstrated objectivity of the results in the spandrel simulation. Furthermore, the comparison between the global response curves obtained with reduced and experimental values of the Young modulus of the bricks confirms the necessity of adjusting the $E_b$-value to achieve a good match with the experiment.

Finally, the model shows satisfactory results in terms of robustness and efficiency: the derived consistent tangent allows for relatively fast simulation times (2:58 hours on a laptop computer with processor 12th Gen Intel(R) Core(TM) i7-1265U 1.80 GHz and RAM 16 GB, and CPU time 12,932 s), enabling implicit micromodelling simulations of full-scale structures under cyclic loads with complex damage-friction interactions.

## 5. Conclusions

An interface material model for quasi-brittle fracture, originally presented in the context of the Discrete Element Method has been improved, implemented in an implicit finite element code and tested to simulate the in-plane behaviour of full-scale masonry structures. In tension-shear, the model is characterized by a cohesive response and accounts for mixed-mode fracture. In compression-shear, cohesion is combined with Coulomb friction in a physically meaningful way. This mixed-mode frictional cohesive zone model allows for a proper description of the cyclic response of masonry material that would not be possible with plasticity-based models characterized by elastic unloading. While previous works introduced a discontinuity in the traction–separation relation to incorporate the frictional term, the present study proposes a regularization of the frictional contribution, together with a consistent linearization of the

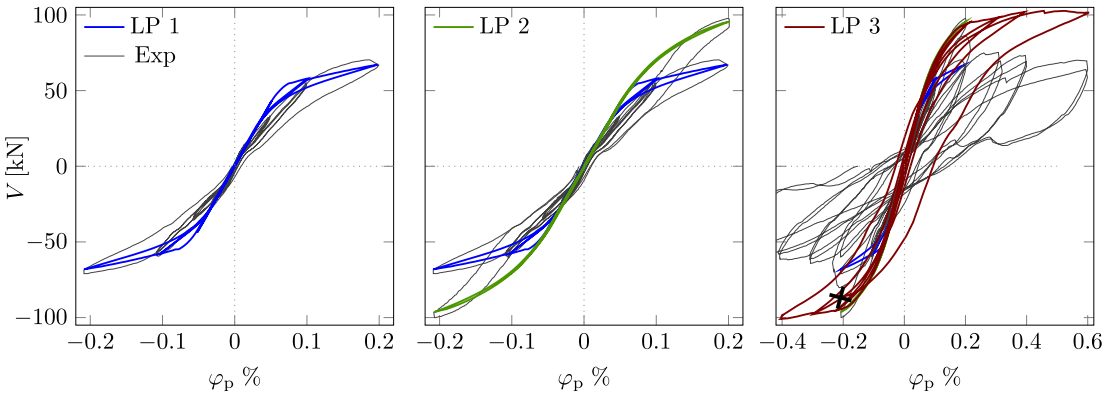


(a) LP 1 (b) LP 1 and 2 (c) LP 1, 2 and 3

**Fig. 20.** Spandrel test: experimental vs numerical global response curves. In (c) a cross indicates the abortion of the analysis. Note that for displaying purposes, different $x$-axis scales are used.

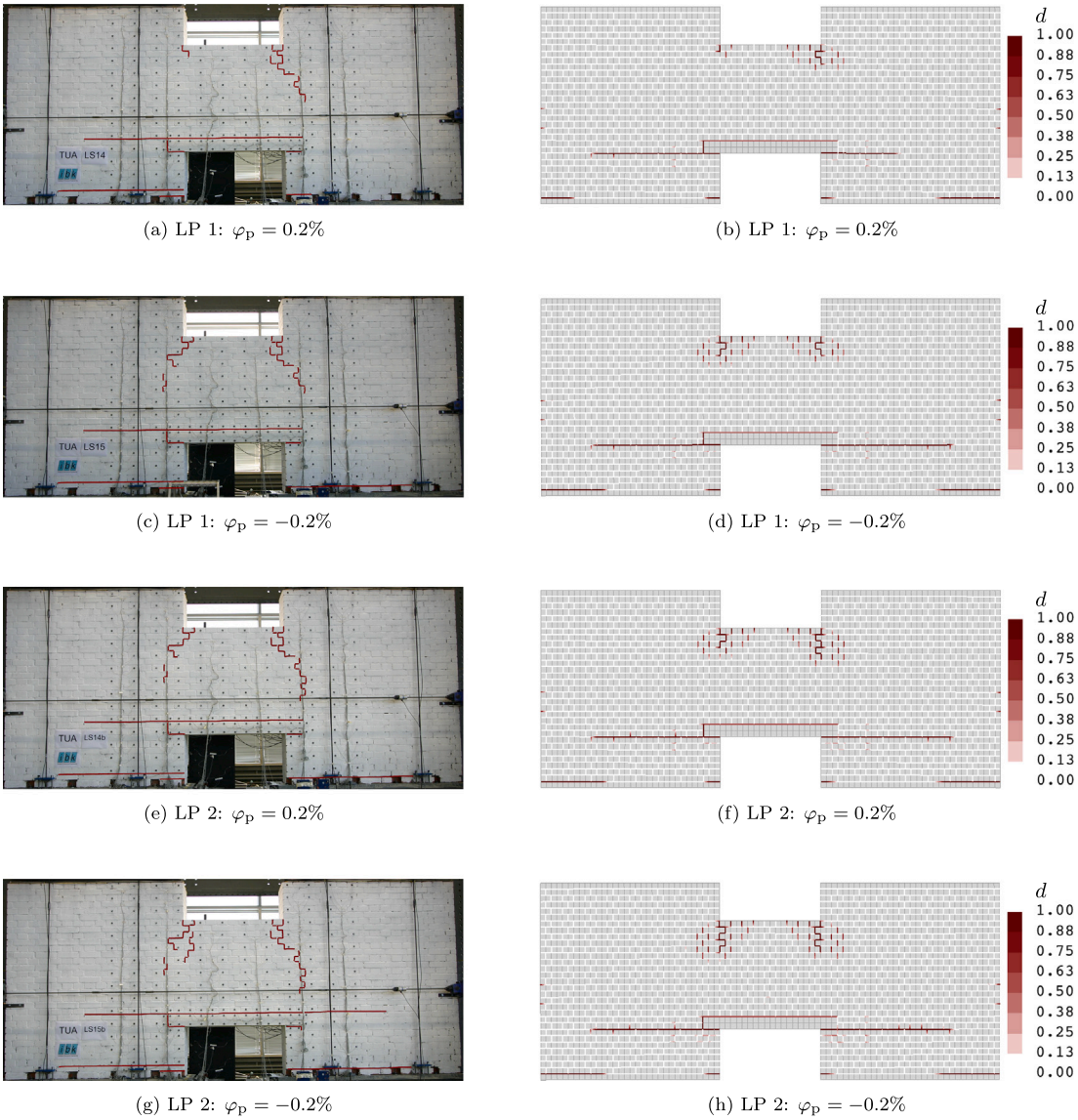


(a) LP 1: $\varphi_p = 0.2\%$ (b) LP 1: $\varphi_p = 0.2\%$

(c) LP 1: $\varphi_p = -0.2\%$ (d) LP 1: $\varphi_p = -0.2\%$

(e) LP 2: $\varphi_p = 0.2\%$ (f) LP 2: $\varphi_p = 0.2\%$

(g) LP 2: $\varphi_p = -0.2\%$ (h) LP 2: $\varphi_p = -0.2\%$

**Fig. 21.** Evolution of the damage for LP 1 and 2: experimental (*left*) versus numerical (*right*). The original pictures are provided by K. Beyer and modified by the authors to highlight the crack pattern.

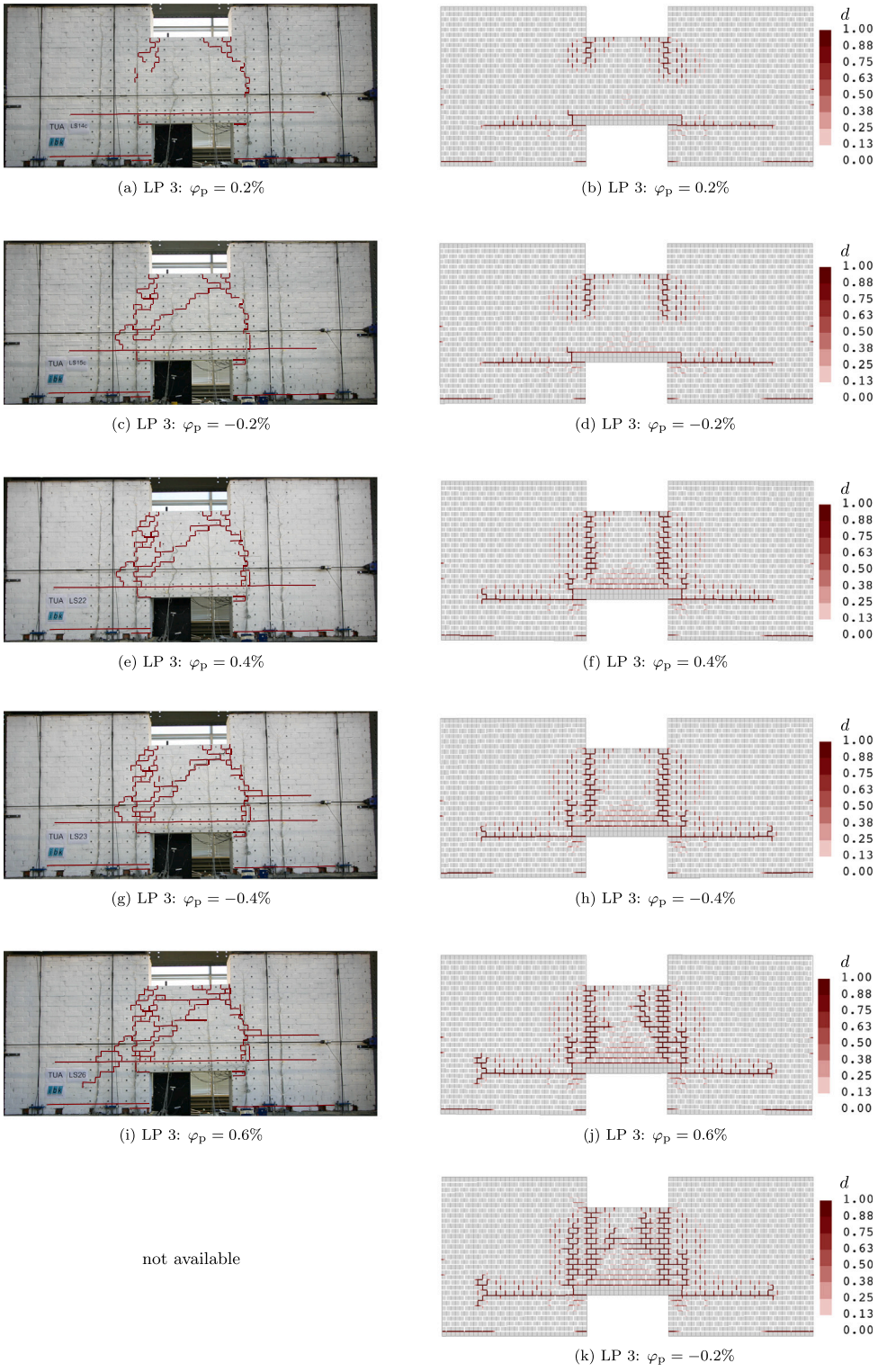


(a) LP 3: $\varphi_p = 0.2\%$ (b) LP 3: $\varphi_p = 0.2\%$

(c) LP 3: $\varphi_p = -0.2\%$ (d) LP 3: $\varphi_p = -0.2\%$

(e) LP 3: $\varphi_p = 0.4\%$ (f) LP 3: $\varphi_p = 0.4\%$

(g) LP 3: $\varphi_p = -0.4\%$ (h) LP 3: $\varphi_p = -0.4\%$

(i) LP 3: $\varphi_p = 0.6\%$ (j) LP 3: $\varphi_p = 0.6\%$

(k) LP 3: $\varphi_p = -0.2\%$

**Fig. 22.** Evolution of the damage for LP 3: experimental (*left*) versus numerical (*right*).

traction update algorithm, to improve the convergence behaviour and enable the analysis of large-scale structures. A new regularization parameter, which determines the degree of approximation of the frictional term to the Coulomb friction, has been introduced. A procedure for calibrating this parameter has been outlined and the robustness of the model has been demonstrated. Sensitivity analyses varying the magnitude of the regularization parameter have been performed to demonstrate that objectivity of the numerical results can be achieved.

The improved model has been applied in a simplified micromodelling approach for the analysis of 2D masonry structures under different cyclic actions: a shear wall subjected to horizontal loading and a spandrel wall subjected to vertical displacements. In the simulation of the shear wall,

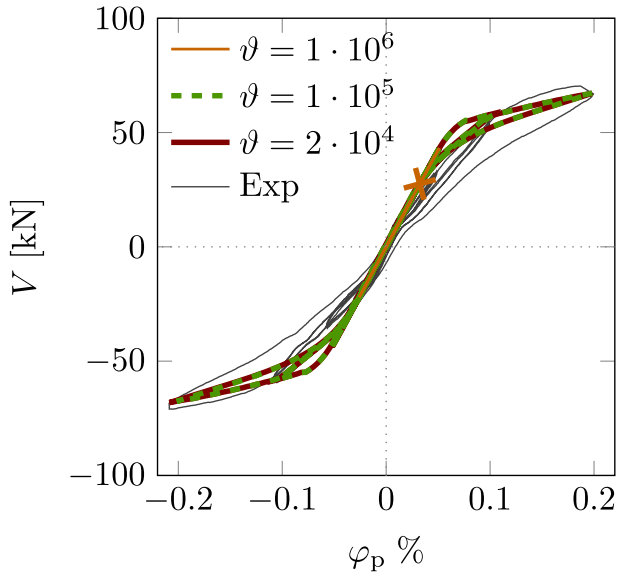


**Fig. 23.** First cycles of the global response curve (LP 1) for different values of the model parameter $\vartheta$. A cross indicates the abortion of the analysis.

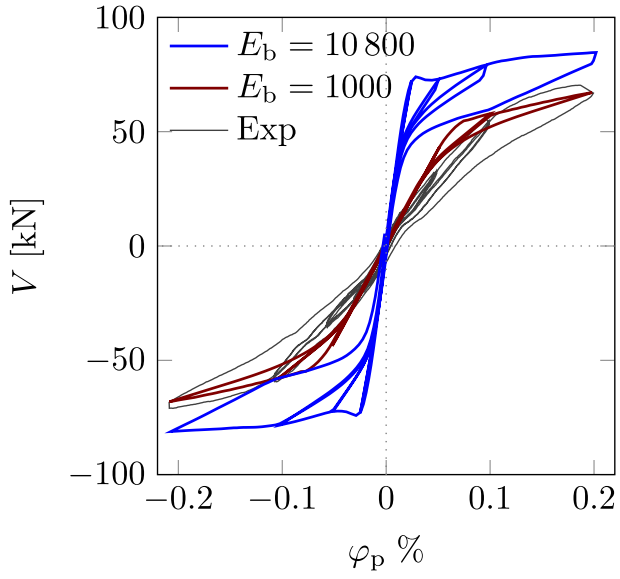


**Fig. 24.** First cycles of the global response curve (LP 1) for different values of the bricks' Young modulus [MPa].

the improved model accurately captures the initial stiffness, capacity, stiffness degradation over cycles, energy dissipation and crack patterns. In the simulation of the spandrel test, discrepancies between the experimental and numerical outcomes have been highlighted. Nevertheless, by considering the experimental uncertainties, the assumptions regarding the material properties and the simplification of the actual geometry of the sample, the model decently describes the mechanical response.

The improved model with consistent tangent stiffness is able to robustly and efficiently simulate the in-plane cyclic response of masonry structures. However, it is worth mentioning that even though the micromodel is computationally efficient, the generation of the numerical model can become expensive if more complex bond patterns and larger structures are analysed. The interaction between decohesion and friction is properly taken into account and the regularization of the frictional term enables robust and accurate implicit micromechanical simulations of complex full-scale masonry walls under cyclic loads.

To conclude, in combination with elastic bricks, the improved interface is able to capture the response of masonry under both tension-shear and compression-shear, provided that the compressive stress does not exceed the strength of the material (compressive crushing). Future perspectives regard the addition of a plastic-damage cap for the phenomenological description of compressive crushing and the extension to 3D for modelling the out-of-plane response of masonry.

## CRediT authorship contribution statement

**G. Cera:** Writing – original draft, Validation, Software, Methodology, Conceptualization. **J.G. Rots:** Writing – review & editing, Supervision, Methodology, Funding acquisition. **A.T. Slobbe:** Writing – review & editing, Supervision, Methodology, Funding acquisition. **F. Messali:** Writing – review & editing, Supervision, Methodology.

## Declaration of competing interest

The authors declare that they have no known competing financial interests or personal relationships that could have appeared to influence the work reported in this paper.

## Acknowledgments

This work was supported by the Netherlands Organization for Applied Scientific Research (TNO) and conducted during the early research program Subsidence and Building Damage. The authors gratefully acknowledge Dr. Katrin Beyer for her assistance in interpreting the experimental data of the spandrel test TUA and for sharing additional documentation about the experimental setup and evolution of the crack pattern. Finally, the first author thanks DIANA FEA BV for its availability and technical support.

## Appendix A. Cohesive constitutive equations

In this Annex, Eqs. (10), (11) and (15) are derived. The procedure follows the same steps as outlined in [35], but with a different definition of the mode-mixity $\beta$ (Eq. 6).

### *A.1. Derivation of the mixed-mode limit elastic displacement jump $[\![u]\!]_m$ (Eq. 11)*

The damage initiation criterion (Eq. 8) can be rewritten in terms of displacement jump components as [35]:

$$\left(\frac{\langle [\![u]\!]_n \rangle}{[\![u]\!]_n^e}\right)^2 + \left(\frac{[\![u]\!]_s}{[\![u]\!]_s^e}\right)^2 = 1 \tag{A.1}$$

Furthermore, by rearranging Eq. (6) and substituting into Eq. (7), the displacement jump components $[\![u]\!]_n$ and $[\![u]\!]_s$ are expressed in terms of the equivalent displacement jump $[\![u]\!]_{eq}$ as:

$$[\![u]\!]_n = \sqrt{1-\beta}\,[\![u]\!]_{eq}; \qquad [\![u]\!]_s = \sqrt{\beta}\,[\![u]\!]_{eq} \tag{A.2}$$

By inserting these expressions into Eq. (A.1), the damage initiation criterion can be rewritten in terms of $[\![u]\!]_{eq}$. The value of $[\![u]\!]_{eq}$ that satisfies the criterion Eq. (A.1) is the mixed-mode limit elastic displacement $[\![u]\!]_m$:

$$[\![u]\!]_m = [\![u]\!]_n^e [\![u]\!]_s^e \sqrt{\frac{1}{\beta\left([\![u]\!]_n^e\right)^2 + (1-\beta)\left([\![u]\!]_s^e\right)^2}} \tag{11}$$

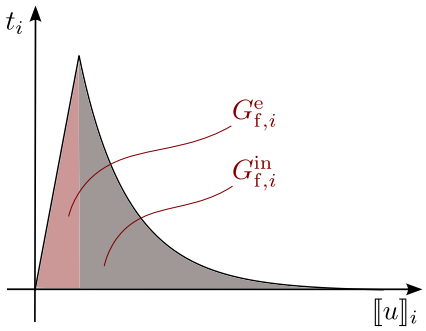


**Fig. A.25.** Cohesive fracture energy for pure-mode $i$ = n, s, divided in elastic and inelastic parts.

### *A.2. Derivation of the mixed-mode strength $f_m$ (Eq. 10)*

Through the relations in Eqs. (11) and (A.2), the traction components at the elastic limit ($d = 0$) are:

$$t^{\mathrm{e}}_{\mathrm{n}} = \sqrt{1-\beta}\, k_{\mathrm{n}} [\![u]\!]_{\mathrm{m}}; \qquad t^{\mathrm{e}}_{\mathrm{s}} = \sqrt{\beta}\, k_{\mathrm{s}} [\![u]\!]_{\mathrm{m}} \tag{A.3}$$

The mixed-mode strength $f_{\mathrm{m}}$ is defined as

$$f_{\mathrm{m}} = \sqrt{(t^{\mathrm{e}}_{\mathrm{n}})^2 + (t^{\mathrm{e}}_{\mathrm{s}})^2} \tag{A.4}$$

Substituting the expressions from Eqs. (11) and (A.3) into Eq. (A.4) yields:

$$f_{\mathrm{m}} = [\![u]\!]^{\mathrm{e}}_{\mathrm{n}} [\![u]\!]^{\mathrm{e}}_{\mathrm{s}} \sqrt{\frac{(1-\beta)\, k_{\mathrm{n}}^2 + \beta\, k_{\mathrm{s}}^2}{\beta \left( [\![u]\!]^{\mathrm{e}}_{\mathrm{n}} \right)^2 + (1-\beta) \left( [\![u]\!]^{\mathrm{e}}_{\mathrm{s}} \right)^2}} \tag{10}$$

### *A.3. Derivation of the ratios $\psi_I$ and $\psi_{II}$ (Eq. 15)*

The cohesive energy, for each mode $i$ = I,II, is defined as the sum of the elastic and inelastic parts (Fig. A.25), indicated by the subscripts “e” and “in”, respectively:

$$G_{\mathrm{f},i} = G^{\mathrm{e}}_{\mathrm{f},i} + G^{\mathrm{in}}_{\mathrm{f},i} \qquad i = \mathrm{I,II} \tag{A.5}$$

The expressions in Eq. (15) are computed by assuming that the ratio of the elastic energy over the total energy during pure-mode fracture is the same as the ratio of the pure-mode components during mixed-mode fracture:

$$\frac{G^{\mathrm{e}}_{\mathrm{f},i}}{G_{\mathrm{f},i}} = \frac{G^{\mathrm{e}}_{\mathrm{f,mix},i}}{G_{\mathrm{f,mix},i}} = \mathrm{const}_i \quad i = \mathrm{I,II} \tag{A.6}$$

Thus, Eq. (14) can be rewritten as:

$$\psi_i = \frac{G_{\mathrm{f,mix},i}}{G_{\mathrm{f},i}} = \frac{G^{\mathrm{e}}_{\mathrm{f,mix},i}}{G^{\mathrm{e}}_{\mathrm{f},i}} \quad i = \mathrm{I,II} \tag{A.7}$$

where

$$G^{\mathrm{e}}_{\mathrm{f,I}} = \frac{f_{\mathrm{n}} [\![u]\!]^{\mathrm{e}}_{\mathrm{n}}}{2}; \quad G^{\mathrm{e}}_{\mathrm{f,II}} = \frac{f_{\mathrm{s}} [\![u]\!]^{\mathrm{e}}_{\mathrm{s}}}{2}; \quad G^{\mathrm{e}}_{\mathrm{f,mix,I}} = \frac{t^{\mathrm{e}}_{\mathrm{n}} [\![u]\!]^{0}_{\mathrm{n}}}{2}; \quad G^{\mathrm{e}}_{\mathrm{f,mix,II}} = \frac{t^{\mathrm{e}}_{\mathrm{s}} [\![u]\!]^{0}_{\mathrm{s}}}{2} \tag{A.8}$$

with $[\![u]\!]^0_{\mathrm{n}}$ and $[\![u]\!]^0_{\mathrm{s}}$ being the components of the mixed-mode limit elastic displacement jump:

$$[\![u]\!]^0_{\mathrm{n}} = \sqrt{1-\beta}\, [\![u]\!]_{\mathrm{m}}; \qquad [\![u]\!]^0_{\mathrm{s}} = \sqrt{\beta}\, [\![u]\!]_{\mathrm{m}} \tag{A.9}$$

Substituting Eqs. (11), (A.8) and (A.9) into Eq. (A.7) gives:

$$\psi_{\mathrm{I}} = \frac{(1-\beta) \left( [\![u]\!]^{\mathrm{e}}_{\mathrm{s}} \right)^2}{(1-\beta) \left( [\![u]\!]^{\mathrm{e}}_{\mathrm{s}} \right)^2 + \beta \left( [\![u]\!]^{\mathrm{e}}_{\mathrm{n}} \right)^2}; \qquad \psi_{\mathrm{II}} = \frac{\beta \left( [\![u]\!]^{\mathrm{e}}_{\mathrm{n}} \right)^2}{(1-\beta) \left( [\![u]\!]^{\mathrm{e}}_{\mathrm{s}} \right)^2 + \beta \left( [\![u]\!]^{\mathrm{e}}_{\mathrm{n}} \right)^2} \tag{15}$$

## Data availability

The data presented in this article can be accessed through the 4TU.ResearchData repository: https://doi.org/10.4121/fcc76932-05e1-46f1-869e-25ab0a09b4f8.

## References


[1] Zucchini A, Lourenço PB. Mechanics of masonry in compression: results from a homogenisation approach. Comput Struct 2007;85(3–4):193–204.

[2] D'Ayala D. Assessing the seismic vulnerability of masonry buildings. Dec 2013. p. 334–65. https://doi.org/10.1533/9780857098986.3.334. ISBN: 9780857092687.

[3] D'Altri A, Sarhosis V, Milani G, Rots J, Cattari S, Lagomarsino S, Sacco E, Tralli A, Castellazzi G, De Miranda S. A review of numerical models for masonry structures. In: Numerical modeling of masonry and historical structures. Elsevier; 2019. p. 3–53. https://doi.org/10.1016/B978-0-08-102439-3.00001-4. ISBN: 978-0-08-102439-3. https://linkinghub.elsevier.com/retrieve/pii/B9780081024393000014.

[4] Boscardin MD, Cording EJ. Building response to excavation-induced settlement. J Geotech Eng 1989:21.

[5] Mair RJ, Taylor RN, Burland JB. Prediction of ground movements and assessment of risk of building damage due to bored tunnelling. In: Geotechnical aspects of underground construction in soft ground (tunnelling '96). Theme: settlement effects of bored tunnels (IS London '96). London, UK: Balkema; 1996. p. 713–8. ISBN: 90-5410-856-8.

[6] Masia MJ, Kleeman PW, Melchers RE. Modeling soil/structure interaction for masonry structures. J Struct Eng Apr 2004;130(4):641–9. https://doi.org/10.1061/(ASCE)0733-9445(2004)130:4(641). ISSN: 0733-9445, 1943-541X. https://ascelibrary.org/doi/10.1061/%28ASCE%290733-9445%282004%29130%3A4%28641%29.

[7] Giardina G, Hendriks MA, Rots JG. Numerical analysis of tunnelling effects on masonry buildings: the influence of tunnel location on damage assessment. In: Structural analysis of historic constructions, vol. 133. Trans Tech Publications Ltd. Oct 2010. p. 289–94. Advanced Materials Research. https://doi.org/10.4028/www.scientific.net/AMR.133-134.289.

[8] Lourenço PB. Analysis of masonry structures with interface elements: theory and applications. Tech. rep. TUD-03-21-22-0-01, TNO-94-NM-R0762. Delft, The Netherlands: Delft University of Technology, Faculty of Civil Engineering; TNO Building and Construction Research. Jun 1994.

[9] Lourenço PB. Computational strategies for masonry structures [Ph.D. thesis]. Delft University of Technology; 1996.

[10] Dugdale D. Yielding of steel sheets containing slits. J Mech Phys Solids May 1960;8(2):100–4. https://doi.org/10.1016/0022-5096(60)90013-2. ISSN: 00225096. https://linkinghub.elsevier.com/retrieve/pii/0022509660900132.

[11] Barenblatt G. The mathematical theory of equilibrium cracks in brittle fracture. In: Advances in applied mechanics, vol. 7. Elsevier; 1962. p. 55–129. https://doi.org/10.1016/S0065-2156(08)70121-2. https://hal.science/hal-03601989.

[12] Dhanasekar M, Page A, Kleeman P. The failure of brick masonry under biaxial stresses. Proc Inst Civ Eng Jun 1985;79(2):295–313. https://doi.org/10.1680/iicep.1985.992. ISSN: 1753-7789. https://www.icevirtuallibrary.com/doi/10.1680/iicep.1985.992.

[13] Hillerborg A, Modéer M, Petersson P-E. Analysis of crack formation and crack growth in concrete by means of fracture mechanics and finite elements. Cem Concr Res Nov 1976;6(6):773–81. https://doi.org/10.1016/0008-8846(76)90007-7. ISSN: 00088846. https://linkinghub.elsevier.com/retrieve/pii/0008884676900077.

[14] Schellekens J, De Borst R. A non-linear finite element approach for the analysis of mode-i free edge delamination in composites. Int J Solids Struct 1993;30(9):1239–53. https://doi.org/10.1016/0020-7683(93)90014-X. ISSN: 00207683. https://linkinghub.elsevier.com/retrieve/pii/002076839390014X.

[15] Alfano G, Crisfield MA. Finite element interface models for the delamination analysis of laminated composites: mechanical and computational issues. Int J Numer Methods Eng Mar. 10 2001;50(7):1701–36. https://doi.org/10.1002/nme.93. ISSN: 0029-5981, 1097-0207. https://onlinelibrary.wiley.com/doi/10.1002/nme.93.

[16] Giambanco G, Mróz Z. The interphase model for the analysis of joints in rock masses and masonry structures. Meccanica 2001;36:111–30.

[17] Turon A, Camanho P, Costa J, Dávila C. A damage model for the simulation of delamination in advanced composites under variable-mode loading. Mech Mater Nov 2006;38(11):1072–89. https://doi.org/10.1016/j.mechmat.2005.10.003. ISSN: 01676636. https://linkinghub.elsevier.com/retrieve/pii/S0167663605002000.

[18] Page A. Finite element model for masonry. J Struct Div ASCE 1978;104:1267–85.

[19] Lotfi HR, Shing PB. Interface model applied to fracture of masonry structures. J Struct Eng Jan 1994;120(1):63–80. https://doi.org/10.1061/(ASCE)0733-9445(1994)120:1(63). URL: https://ascelibrary.org/doi/10.1061/%28ASCE%290733-9445%281994%29120%3A1%2863%29. ISSN: 0733-9445, 1943-541X.

[20] Lourenço PB, Rots JG, Blaauwendraad J. Two approaches for the analysis of masonry structures: micro and Macro-Modeling. HERON 1995;40(4):313–40. ISSN: 0046-7316.

[21] Lourenço PB, Rots JG. Multisurface interface model for analysis of masonry structures. J Eng Mech Jul 1997;123(7):660–8. https://doi.org/10.1061/(ASCE)0733-9399. ISSN: 0733-9399, 1943-7889. URL: https://ascelibrary.org/doi/10.1061/%28ASCE%290733-9399%281997%29123%3A7%28660%29.

[22] Van Zijl G, De Borst R, Rots J. The role of crack rate dependence in the long-term behaviour of cementitious materials. Int J Solids Struct Jul

2001;38(30):5063–79. https://doi.org/10.1016/S0020-7683(00)00338-3. ISSN: 00207683. https://linkinghub.elsevier.com/retrieve/pii/S0020768300003383.
[23] Giambanco G, Rizzo S, Spallino R. Numerical analysis of masonry structures via interface models. Comput Methods Appl Mech Eng Oct 2001;190(49):6493–511. https://doi.org/10.1016/S0045-7825(01)00225-0. ISSN: 00457825. https://linkinghub.elsevier.com/retrieve/pii/S0045782501002250.
[24] Van Zijl PAG. Modeling masonry shear-compression: role of dilatancy highlighted. J Eng Mech Nov 2004;130(11):1289–96. https://doi.org/10.1061/(ASCE)0733-9399(2004)130:11(1289). URL: https://ascelibrary.org/doi/10.1061/%28ASCE%290733-9399%282004%29130%3A11%281289%29. ISSN: 0733-9399, 1943-7889.
[25] Oliveira D, Lourenço P. Implementation and validation of a constitutive model for the cyclic behaviour of interface elements. Comput Struct Jul 2004;82(17):1451–61. https://doi.org/10.1016/j.compstruc.2004.03.041. ISSN: 00457949. https://linkinghub.elsevier.com/retrieve/pii/S0045794904001312.
[26] Chaimoon K, Attard MM. Modeling of unreinforced masonry walls under shear and compression. Eng Struct Sept 2007;29(9):2056–68. https://doi.org/10.1016/j.engstruct.2006.10.019. ISSN: 01410296. https://linkinghub.elsevier.com/retrieve/pii/S0141029606004305.
[27] Macorini L, Izzuddin B. Nonlinear analysis of masonry structures using mesoscale partitioned modelling. Adv Eng Softw Jun 2013;60-61:58–69. https://doi.org/10.1016/j.advengsoft.2012.11.008. ISSN: 09659978. https://linkinghub.elsevier.com/retrieve/pii/S096599781200155X.
[28] Tvergaard V. Effect of fibre debonding in a whisker-reinforced metal. Mater Sci Eng A Jun 1990;125(2):203–13. https://doi.org/10.1016/0921-5093(90)90170-8. ISSN: 09215093. https://linkinghub.elsevier.com/retrieve/pii/0921509390901708.
[29] Gambarotta L, Lagomarsino S. Damage models for the seismic response of brick masonry shear walls. Part I: the Mortar Joint model and its applications. Earthq Eng Struct Dyn Apr 1997;26(4):423–39. ISSN: 0098-8847, 1096-9845. https://onlinelibrary.wiley.com/doi/10.1002/%28SICI%291096-9845%28199704%2926%3A4%3C423%3A%3AID-EQE650%3E3.0.CO%3B2-%23.
[30] Raous M, Monerie Y. Unilateral contact, friction and adhesion: 3d cracks in composite materials. In: Contact mechanics, vol. 333. Dordrecht: Springer Netherlands; 2002. p. 333–346. isbn: 978-94-017-1154-8.
[31] Alfano G, Sacco E. Combining interface damage and friction in a cohesive-zone model. Int J Numer Methods Eng Oct. 29 2006;68(5):542–82. https://doi.org/10.1002/nme.1728. URL: https://onlinelibrary.wiley.com/doi/10.1002/nme.1728. ISSN: 00295981.
[32] Snozzi L, Molinari J-F. A cohesive element model for mixed mode loading with frictional contact capability. Int J Numer Methods Eng Feb. 3 2013;93(5):510–26. https://doi.org/10.1002/nme.4398. URL: https://onlinelibrary.wiley.com/doi/10.1002/nme.4398. ISSN: 0029-5981, 1097-0207.
[33] D'Altri AM, De Miranda S, Castellazzi G, Sarhosis V. A 3d detailed micro-model for the in-plane and out-of-plane numerical analysis of masonry panels. Comput Struct Aug 2018;206:18–30. https://doi.org/10.1016/j.compstruc.2018.06.007. ISSN: 00457949. https://linkinghub.elsevier.com/retrieve/pii/S0045794918301172.
[34] Parrinello F, Failla B, Borino G. Cohesive–frictional interface constitutive model. Int J Solids Struct Jun 2009;46(13):2680–92. https://doi.org/10.1016/j.ijsolstr.2009.02.016. ISSN: 00207683. https://linkinghub.elsevier.com/retrieve/pii/S0020768309000900.
[35] Venzal V, Morel S, Parent T, Dubois F. Frictional cohesive zone model for quasi-brittle fracture: mixed-mode and coupling between cohesive and frictional behaviors. Int J Solids Struct Aug 2020;198:17–30. https://doi.org/10.1016/j.ijsolstr.2020.04.023. ISSN: 00207683. https://linkinghub.elsevier.com/retrieve/pii/S0020768320301402.
[36] Sacco E, Toti J. Interface elements for the analysis of masonry structures. Int J Comput Methods Eng Sci Mech 2010;11(6):354–73. https://doi.org/10.1080/15502287.2010.516793. ISSN: 15502295.
[37] Camanho P, Davila CG, De Moura MF. Numerical simulation of Mixed-Mode progressive delamination in composite materials. J Compos Mater Aug 2003;37(16):1415–38. https://doi.org/10.1177/0021998303034505. ISSN: 0021-9983, 1530-793X. https://journals.sagepub.com/doi/10.1177/0021998303034505.
[38] Boukham A, Venzal V, Parent T, Morel S, Dubois F, Solbes B. 3d hybrid modeling approach combining the finite and discrete element methods: validation based on masonry shear wall tests. Int J Solids Struct Mar 2024;289:112638. https://doi.org/10.1016/j.ijsolstr.2023.112638. ISSN: 00207683. https://linkinghub.elsevier.com/retrieve/pii/S0020768323005358.
[39] Raous M, Panagiotopoulos PD. Quasistatic signorini problem with Coulomb friction and coupling to adhesion. In Wriggers P, editor. New developments in contact problems, vol. 384. CISM Courses and Lectures. Vienna: Springer-Verlag; 1999. p. 101–78.
[40] González E, Maimí P, Turon A, Renart J. Simulation of delamination by means of cohesive elements using an explicit finite element code. Comput Mater Continua Jan 2009;9:51–92. https://doi.org/10.3970/cmc.2009.009.051.
[41] Brewer JC, Lagace PA. Quadratic stress criterion for initiation of delamination. J Compos Mater 1988;22(12):1141–55. https://doi.org/10.1177/002199838802201205
[42] Korswagen PA, Longo M, Meulman E, Rots JG. Crack initiation and propagation in unreinforced masonry specimens subjected to repeated in-plane loading during light damage. Bull Earthq Eng Aug 2019;17(8):4651–87. https://doi.org/10.1007/s10518-018-00553-5. ISSN: 1570-761X, 1573-1456. http://link.springer.com/10.1007/s10518-018-00553-5.
[43] Korswagen PA, Longo M, Meulman E, van Hoogdalem C. Damage sensitivity of Groningen masonry structures - experimental and computational studies, C31B69WP0-12. Delft University of Technology, Dec. 30, 2017.
[44] Rots JG. In Civieltechnisch Centrum Uitvoering Research en Regelgeving, editor. Structural masonry: an experimental/numerical basis for practical design rules. Rotterdam: Balkema; 1997. 152 pp. isbn: 978-90-5410-680-7.
[45] Jafari S, Rots JG, Esposito R, Messali F. Characterizing the material properties of Dutch unreinforced masonry. Procedia Eng 2017;193:250–7. https://doi.org/10.1016/j.proeng.2017.06.211. ISSN: 18777058. https://linkinghub.elsevier.com/retrieve/pii/S1877705817327674.
[46] Jafari S. Material characterisation of existing masonry a strategy to determine strength, stiffness and toughness properties for structural analysis [Ph.D. thesis]. TU Delft; 2021.
[47] Hallett SR, Wisnom MR. Numerical investigation of progressive damage and the effect of layup in notched tensile tests. J Compos Mater Jul 2006;40(14):1229–45. https://doi.org/10.1177/0021998305057432. ISSN: 0021-9983, 1530-793X. https://journals.sagepub.com/doi/10.1177/0021998305057432.
[48] Rots G. Computational modeling of concrete fracture [Ph.D. thesis]. Delft University of Technology; 1988.
[49] Schellekens JCJ, De Borst R. On the numerical integration of interface elements. Int J Numer Methods Eng Jan. 15 1993;36(1):43–66. https://doi.org/10.1002/nme.1620360104. ISSN: 0029-5981, 1097-0207. https://onlinelibrary.wiley.com/doi/10.1002/nme.1620360104.
[50] Hendry AW. Structural masonry. London: Macmillan Education UK; 1981. https://doi.org/10.1007/978-1-349-81439-8_2. isbn: 978-1-349-81439-8.
[51] Beyer K, Abo-El-Ezz A, Dazio A. Quasi-static cyclic tests on different types of masonry spandrels. IBK Report 327. ETH Zürich, Switzerland: Institute of Structural Engineering; 2010.
[52] Beyer K, Dazio A. Quasi-Static monotonic and cyclic tests on composite spandrels. Earthq Spectra Aug 2012;28(3):885–906. https://doi.org/10.1193/1.4000058. URL: http://journals.sagepub.com/doi/10.1193/1.4000058. ISSN: 8755-2930, 1944-8201.
[53] Beyer K, Dazio A. Quasi-Static cyclic tests on masonry spandrels. Earthq Spectra Aug 2012;28(3):907–29. https://doi.org/10.1193/1.4000063. ISSN: 8755-2930, 1944-8201. http://journals.sagepub.com/doi/10.1193/1.4000063.
[54] Mirra M, Ravenshorst G, de Vries P, Messali F. Experimental characterisation of as-built and retrofitted timber-masonry connections under monotonic, cyclic and dynamic loading. Constr Build Mater 2022;358:129446. https://doi.org/10.1016/j.conbuildmat.2022.129446. ISSN: 0950-0618. https://www.sciencedirect.com/science/article/pii/S0950061822031026.
[55] Arslan O, Messali F, Smyrou E, Bal, Rots J. Characterisation of timber joists-masonry connections in double-leaf cavity walls – part 1: experimental results. Structures Oct 2024;68:107164. https://doi.org/10.1016/j.istruc.2024.107164